*Journal of Computational and Applied Mechanics, Vol. 18, No. 1, (2023), pp. 3–34*
DOI: 10.32973/jcam.2023.001

# STRESS-BASED DIMENSIONAL REDUCTION AND DUAL-MIXED *hp* FINITE ELEMENTS FOR ELASTIC PLATES

Edgár Bertóti
Institute of Applied Mechanics, University of Miskolc
H-3515 Miskolc-Egyetemváros, Hungary
edgar.bertoti@uni-miskolc.hu

[Received: November 1, 2022; Accepted: February 13, 2023]

**Abstract.** Starting from the linearized weak forms of the kinematic equation and the angular momentum balance equation of three-dimensional non-linear elasticity, a stress-based dimensional reduction procedure is presented for elastic plates. After expanding the three-dimensional non-symmetric stress tensor into power series with respect to the thickness coordinate, the translational equilibrium equations, written in terms of the expanded stress coefficients, are satisfied by introducing first-order stress functions. The symmetry of the stress field is satisfied in a weak sense by applying the material rotations as Lagrangian multipliers. The seven-field plate model developed in this way employs unmodified three-dimensional strain-stress relations.

On the basis of the dimensionally reduced plate model derived, a new dual-mixed plate bending finite element model is developed and presented. The numerical performance of the *hp*-version plate elements is investigated through the solutions of standard plate bending problems. It is shown that the modeling error of the stress-based plate model in the energy norm is better than that of the displacement-based Kirchhoff- and Reissner-Mindlin plate models. The numerical solutions and their comparisons to reference solutions indicate that the dual-mixed *hp* elements are free from locking problems, in either the energy norm or the stress computations, both for *h*- and *p*-extensions, and the results obtained for the stresses are accurate and reliable even for extremely thin plates.

*Mathematical Subject Classification:* 05C38, 15A15
*Keywords*: plate model, dimensional reduction, stress-based approach, dual-mixed weak formulation, locking-free *hp* finite element

## 1. Introduction

The finite element modeling of structural plate and shell problems has a long history and several successful formulations exist and are being used today in commercial finite element codes. The majority of the plate and shell elements are displacement-based ones and they usually rely on some assumptions regarding the transverse variation of the displacement components. Classical plate and shell theories, applying either the Kirchhoff–Love- or the Reissner–Mindlin hypothesis, with respect to the motion of the normal to the middle surface, are often called first-order theories [1].

There are two main directions in the construction of plate and shell finite elements: discretization based on dimensionally reduced theories leading to two-dimensional surface elements and continuum-based formulations leading to solid-shell, or degenerated

three-dimensional, elements. Hierarchic sequences of plate and shell models and elements can also be constructed within the framework of either of these two modeling directions [2, 3].

Considering the approach of dimensional reduction, the first-order shear deformation models and elements with Reissner–Mindlin kinematics are the most popular ones. This is primarily due to the fact that they require $C_0$-continuous approximation of the displacement variables, in contrast to the $C_1$-continuity requirement of the elements with Kirchhoff–Love kinematics. It is also well-known that when low-order polynomial approximation is used for the displacements in these plate and shell elements, some inconsistencies in the representation of the transverse shear and membrane energies are introduced through the discretization, and the elements can exhibit different kind of numerical over-stiffening problems, usually called locking [2, 3]. Although the resolution of transverse shear locking and membrane locking in plate and shell elements has been the subject of intensive research in the last decades, and several successful strategies and techniques have been developed to alleviate locking, the improvement and stabilization of the low-order elements based on first-order plate and shell theories seems to be a never-ending story, see, e.g, [4, 5]. In the framework of the displacement-based formulations, higher-order approximations and the $p$-version of the finite element method are among the most reliable strategies for avoiding numerical convergence problems [6–9].

Considering the direction of the solid-shell approach, the plate and shell elements are usually deduced from continuum-based three-dimensional or solid finite elements [10, 11]. One of the main advantages of this formulation is the applicability of unmodified three-dimensional constitutive equations, in contrast to the dimensionally reduced first-order models, where the inconsistencies due to the kinematical constraints require the modification of the original three-dimensional constitutive equations. However, the solid-shell elements are not exempt from different kinds of numerical locking problems, either. In addition to the shear- and membrane locking, known from dimensionally reduced models, thickness locking, trapezoidal locking and incompressibility locking can also be present, especially when low-order approximation is used [11]. Although the research efforts spent for solving these problems has resulted in successful solutions, the improvement of solid-shell elements is still an active research area [4, 12].

Mixed-hybrid formulations and finite elements for plates and shells are usually based on a Hu–Washizu or Hellinger–Reissner type, primal-mixed or dual-mixed, variational principle. These formulations have also been intensively researched in the last few decades, especially because the elements of these types are proven or assumed to be exempt from numerical locking problems. The price for that is a larger number of independently approximated variables. An additional difficulty is that mixed-hybrid formulations require the choice of stable approximation spaces for the simultaneously approximated kinematic and stress variables [13]. It has also been long recognized that the majority of the modified and locking-free displacement-based plate and shell elements are equivalent or strongly related to elements deduced from mixed variational principles [1, 14].

Primal-mixed formulations and finite elements with continuous displacements and discontinuous surface tractions are much more popular than dual-mixed formulations and elements with continuous surface tractions and discontinuous displacements. This is partly due to fact that dual-mixed models and elements are more sophisticated, both theoretically and computationally, than the primal-mixed ones. An additional difficulty with dual-mixed models is their limited applicability to non-linear problems, as they rely on a complementary energy potential that should be expressed in terms of stresses. This may require the inversion of a general non-linear strain-stress relation, which can be a rather complicated task, if possible at all.

Dual-mixed elements can be formulated with either symmetric or non-symmetric stresses as primarily approximated variables. When symmetric stresses are used, the main problem is finding stable approximation spaces for them, even in the case of two-dimensional elasticity problems. This difficulty can be traced back to the construction of equilibrium elements with symmetric stresses, requiring $C_1$-continuous approximation for the second-order stress functions [15]. One resolution for this problem is to use dual-mixed variational principles with non-symmetric stresses and the symmetry of the stress tensor, the balance of angular momentum, is enforced then in a weak sense by applying the material rotations as Lagrangian multipliers [15, 16]. Finding stable approximation spaces for dual-mixed elements with non-symmetric stress space is relatively easy [17], which may be related to the fact that an equilibrated but non-symmetric stress field can be generated by $C_0$-continuous first-order stress functions. The stress boundary conditions in dual-mixed formulations are essential conditions and the related requirement of surface traction continuity is usually satisfied by employing hybridization techniques [13, 18].

The developments to be presented in this paper belong to a special research direction, the aim of which is the development of stress-based dimensionally reduced models for plates and shells using dual-mixed weak formulations with non-symmetric stress space. These models do not rely on the classical kinematical hypotheses and cannot be considered as stress resultant-based formulations. Instead, the stress space is directly approximated across the thickness by (truncated) power series, and the finite element model is based on a dual-mixed variational principle of Hellinger–Reissner or Fraeijs de Veubeke type. The former is a three-field principle and enforces both translational and rotational equilibrium in a weak sense, while the latter is a two-field principle and relies on equilibrated stress space, generated by first-order stress functions, and only the symmetry of the stress space is enforced weakly. Inter-element equilibrium, i.e., surface traction continuity, is satisfied by the related finite elements, and the numerical results are obtained directly for the approximated stress or stress-function variables.

Applying the two-field dual-mixed variational principle of Fraeijs de Veubeke, a dimensionally reduced plate model has already been derived in [19], but only the membrane problem was investigated by two-dimensional *hp* finite elements. Stress-based dimensionally reduced models and *hp* finite elements for axisymmetric problems of cylindrical shells have been presented by [20] using Fraeijs de Veubeke's two-field principle, and by [21] using the three-field dual-mixed principle of Hellinger–Reissner.

The performance of these two types of *hp* finite element models was compared in [22]. A stress-based dimensional reduction procedure based on Hellinger–Reissner's three-field principle, and the related dual-mixed *hp* finite elements for shells of revolution were developed in [23] for elastostatic problems, and in [24] for natural frequency analysis.

The starting point of the formulation and developments reported in this paper is the three-dimensional weak forms of the kinematic equation and the angular momentum balance equation of non-linear elasticity, summarized in Section 2. Following their consistent linearization, the dimensional reduction procedure for elastic plates in terms of stresses is presented in Section 3. Section 4 gives a brief description of the dual-mixed plate bending finite element formulation and the choice of stable approximation spaces for the first-order stress functions and the rotations. The performance and the capabilities of the stress-based plate model and the dual-mixed *hp* finite elements are investigated in Section 5 through the numerical solutions of well-known plate benchmark problems.

## 2. Preliminaries, strong and weak formulation

This section summarizes the strong formulation of non-linear elasticity in material description and recalls the weak forms of the kinematic equation and the balance of angular momentum, including their consistent linearization. Both symbolic and index notation of tensors will be used. Latin tensor indices are assumed to range over 1,2,3 and the Greek indices over 1 and 2. When index notation is used, the summation convention is applied. The scalar product between two tensors is indicated by one dot and the inner product is denoted by a colon. The tensorial product between two tensors of any order has no special sign.

### 2.1. Strong formulation using material description.

The motion of the elastic body is investigated in a Cartesian reference frame. The initial configuration of the body is denoted by ${}^0V$ and its boundary by ${}^0S$ with outward unit normal ${}^0\boldsymbol{n}$. The position of a material point in the stress-free initial configuration is denoted by ${}^0\boldsymbol{x} = {}^0x_i\,\boldsymbol{e}_i$ and in the current deformed configuration by $\boldsymbol{x} = x_i\,\boldsymbol{e}_i$, where ${}^0x_i$ and $x_i$ are the material and spatial coordinates of the same material point and $\boldsymbol{e}_i$ are the orthonormal base vectors. The differential operator with respect to the material coordinates is denoted by ${}^0\nabla = (\partial\,/\partial\,{}^0x_i)\,\boldsymbol{e}_i$.

Applying material description, the governing equations of a nonlinear boundary-value problem in three-dimensional elasticity are

- the kinematic equation:
$$\boldsymbol{F} = \mathbf{1} + \boldsymbol{u}\,{}^0\nabla, \tag{2.1}$$
where $\boldsymbol{F} = \boldsymbol{x}\,{}^0\nabla$ is the deformation gradient with determinant $J = \det \boldsymbol{F} > 0$, $\mathbf{1}$ is the second-order unit tensor and $\boldsymbol{u} = \boldsymbol{x} - {}^0\boldsymbol{x}$ is the displacement vector;
- the general form of the constitutive equation:
$$\boldsymbol{P} = \boldsymbol{P}(\boldsymbol{F}), \tag{2.2}$$
where $\boldsymbol{P}$ is the first Piola-Kirchhoff stress tensor;

- the balance of linear momentum (translational equilibrium equation):

$$\boldsymbol{P} \cdot {}^0\nabla + {}^0\rho \boldsymbol{b} = \boldsymbol{0}, \tag{2.3}$$

  where ${}^0\rho$ is the reference density and $\boldsymbol{b}$ is the prescribed body force density per unit mass;
- the balance of angular momentum (rotational equilibrium equation):

$$\boldsymbol{P} \cdot \boldsymbol{F}^T - \boldsymbol{F} \cdot \boldsymbol{P}^T = \boldsymbol{0}, \tag{2.4}$$

  where a $T$ in the right superscript refers to the transpose; this equation expresses the symmetry of the Cauchy stress tensor $\boldsymbol{\sigma} = J^{-1}\boldsymbol{P} \cdot \boldsymbol{F}^T$.

The boundary conditions to the above system of partial differential equations are the displacement boundary conditions

$$\boldsymbol{u} = \widetilde{\boldsymbol{u}}\,, \qquad {}^0\boldsymbol{x} \in {}^0S_u\,, \tag{2.5}$$

and the stress boundary conditions

$$\boldsymbol{P} \cdot {}^0\boldsymbol{n} = {}^0\widetilde{\boldsymbol{p}}\,, \qquad {}^0\boldsymbol{x} \in {}^0S_p\,, \tag{2.6}$$

where $\widetilde{\boldsymbol{u}}$ is the prescribed displacement vector on ${}^0S_u$ and ${}^0\widetilde{\boldsymbol{p}}$ is the prescribed traction vector on ${}^0S_p$, where ${}^0S_u \cup {}^0S_p = {}^0S$ and ${}^0S_u \cap {}^0S_p = \emptyset$.

2.2. **Angular momentum balance and constitutive equation in terms of the Biot stress tensor.** The polar decomposition of the deformation gradient is given by

$$\boldsymbol{F} = \boldsymbol{R} \cdot \boldsymbol{U}, \tag{2.7}$$

where $\boldsymbol{R}$ is the orthogonal rotation tensor ($\boldsymbol{R}^T \cdot \boldsymbol{R} = \boldsymbol{1}$, $\det \boldsymbol{R} = 1$) and $\boldsymbol{U}$ is the symmetric right stretch tensor. The polar decomposition of the first Piola–Kirchhoff stress tensor $\boldsymbol{P}$ reads

$$\boldsymbol{P} = \boldsymbol{R} \cdot \boldsymbol{T}, \tag{2.8}$$

where $\boldsymbol{R}$ is the same orthogonal rotation tensor that appears in (2.7) and $\boldsymbol{T}$ is the (generally non-symmetric) Biot stress tensor.

The spatial Kirchhoff stress tensor $J\boldsymbol{\sigma}$ can be expressed by the Biot stress tensor and the right stretch tensor as

$$J\boldsymbol{\sigma} = \boldsymbol{P} \cdot \boldsymbol{F}^T = \boldsymbol{R} \cdot (\boldsymbol{T} \cdot \boldsymbol{U}) \cdot \boldsymbol{R}^T, \tag{2.9}$$

and the rotated Kirchhoff stress tensor is given by

$$\boldsymbol{R}^T \cdot (J\boldsymbol{\sigma}) \cdot \boldsymbol{R} = \boldsymbol{T} \cdot \boldsymbol{U}. \tag{2.10}$$

In view of (2.9)–(2.10), the material form of the balance of angular momentum (2.4) can be written in terms of $\boldsymbol{U}$ and $\boldsymbol{T}$ as

$$\boldsymbol{T} \cdot \boldsymbol{U} - \boldsymbol{U} \cdot \boldsymbol{T}^T = \boldsymbol{0}. \tag{2.11}$$

For the special case of isotropic materials $\boldsymbol{T}$ and $\boldsymbol{U}$ are coaxial and $\boldsymbol{T}$ is symmetric.

The right stretch tensor $\boldsymbol{U}$ and the Biot stress tensor $\boldsymbol{T}$ are work-conjugate strain and stress measures and the constitutive relation between them is uniquely invertible [25]. The inverse constitutive equation for the right stretch tensor can be given as

$$\boldsymbol{U} = \boldsymbol{U}(\boldsymbol{T}), \tag{2.12}$$

and the fourth-order tangent compliance tensor is defined by

$$\mathbb{C}^{-1} = \frac{\partial \boldsymbol{U}}{\partial \boldsymbol{T}}, \qquad \mathbb{C}^{-1}_{ijk\ell} = \frac{\partial U_{ij}}{\partial T_{k\ell}} \tag{2.13}$$

with major and minor symmetries $\mathbb{C}^{-1}_{ijk\ell} = \mathbb{C}^{-1}_{k\ell ij} = \mathbb{C}^{-1}_{ij\ell k}$.

2.3. **Weak forms of the kinematic equation.** The dual-mixed weak formulation applied in this paper is based on the weak forms of the kinematic equation (2.1) and the rotational equilibrium equation (2.11). The independent variables are the first Piola–Kirchhoff stress tensor $\boldsymbol{P}$ and the orthogonal rotation tensor $\boldsymbol{R}$.

Taking into account the polar decomposition (2.7) of the deformation gradient, the first weak form of the kinematic equation (2.1) can be written as

$$\delta \mathcal{W}_{K} = \int_{{}^0V} \delta \boldsymbol{P} : (\boldsymbol{R} \cdot \boldsymbol{U} - \boldsymbol{1} - \boldsymbol{u}\, {}^0\nabla)\, \mathrm{d}\, {}^0V = 0, \tag{2.14}$$

where $\delta \boldsymbol{P}$ is an arbitrary but differentiable tensorial test function called the virtual first Piola–Kirchhoff stress tensor. Applying the divergence theorem, the second weak form of (2.1) is obtained from (2.14) as

$$\delta \mathcal{W}_{K} = \int_{{}^0V} \left[\, \delta \boldsymbol{P} : (\boldsymbol{R} \cdot \boldsymbol{U} - \boldsymbol{1}) + (\delta \boldsymbol{P} \cdot {}^0\nabla) \cdot \boldsymbol{u} \,\right] \mathrm{d}\, {}^0V - \int_{{}^0S} \boldsymbol{u} \cdot \delta \boldsymbol{P} \cdot {}^0\boldsymbol{n}\, \mathrm{d}\, {}^0S = 0. \tag{2.15}$$

The displacements can be eliminated from (2.15) by prescribing the constraint equations

$$\delta \boldsymbol{P} \cdot {}^0\nabla = \boldsymbol{0}, \qquad {}^0\boldsymbol{x} \in {}^0V\,, \tag{2.16}$$

$$\delta \boldsymbol{P} \cdot {}^0\boldsymbol{n} = \boldsymbol{0}, \qquad {}^0\boldsymbol{x} \in {}^0S_p \tag{2.17}$$

on $\delta \boldsymbol{P}$, i.e., the virtual first Piola–Kirchhoff stress tensor is assumed to satisfy the homogeneous equilibrium equation (2.16) and the stress boundary condition (2.17). Making use of the displacement boundary condition (2.5) and (2.16)–(2.17), equation (2.15) transforms into

$$\delta \mathcal{W}_{K}(\boldsymbol{P}, \boldsymbol{R}, \delta \boldsymbol{P}) = \int_{{}^0V} \delta \boldsymbol{P} : (\boldsymbol{R} \cdot \boldsymbol{U} - \boldsymbol{1})\, \mathrm{d}\, {}^0V \; - \int_{{}^0S_u} \widetilde{\boldsymbol{u}} \cdot \delta \boldsymbol{P} \cdot {}^0\boldsymbol{n}\, \mathrm{d}\, {}^0S = 0. \tag{2.18}$$

2.4. **Weak forms of the angular momentum balance.** The weak form of the symmetry condition (2.4) for the Cauchy stress tensor can be given by

$$\delta \mathcal{W}_{S} = \int_{{}^0V} \delta \boldsymbol{\Omega} : (\boldsymbol{P} \cdot \boldsymbol{F}^T)\, \mathrm{d}\, {}^0V = 0, \tag{2.19}$$

where $\delta \boldsymbol{\Omega}$ is an arbitrary skew-symmetric tensor called the virtual spatial spin tensor. Taking into account the polar decompositions (2.7) and (2.8), we can write:

$$\delta \boldsymbol{\Omega} : (\boldsymbol{P} \cdot \boldsymbol{F}^T) = \delta \boldsymbol{\Omega} : (\boldsymbol{R} \cdot \boldsymbol{T} \cdot \boldsymbol{U} \cdot \boldsymbol{R}^T) = (\boldsymbol{R}^T \cdot \delta \boldsymbol{\Omega} \cdot \boldsymbol{R}) : (\boldsymbol{T} \cdot \boldsymbol{U}), \tag{2.20}$$

and the weak form of the angular momentum balance (2.19) can be written as

$$\delta \mathcal{W}_{S}(\boldsymbol{P}, \boldsymbol{R}, \delta \boldsymbol{R}) = \int_{{}^0V} \delta \boldsymbol{\Theta} : (\boldsymbol{T} \cdot \boldsymbol{U})\, \mathrm{d}\, {}^0V = 0, \tag{2.21}$$

where $\delta\boldsymbol{\Theta} = \boldsymbol{R}^T \cdot \delta\boldsymbol{\Omega} \cdot \boldsymbol{R}$ is an arbitrary skew-symmetric tensor called the virtual material spin tensor. The virtual spin tensors $\delta\boldsymbol{\Omega}$ and $\delta\boldsymbol{\Theta}$ are related to the virtual rotation tensor $\delta\boldsymbol{R}$ as

$$\delta\boldsymbol{\Omega} = \delta\boldsymbol{R} \cdot \boldsymbol{R}^T, \qquad \delta\boldsymbol{\Theta} = \boldsymbol{R}^T \cdot \delta\boldsymbol{R}. \tag{2.22}$$

When the rotation tensor $\boldsymbol{R}$ is parameterized by a rotation vector $\boldsymbol{\phi}$, according to

$$\boldsymbol{R}(\boldsymbol{\phi}) = \exp(\boldsymbol{\phi} \times \mathbf{1}), \tag{2.23}$$

the relation between the spatial and the material spin tensors in (2.22) can be given as [14, 26, 27]

$$\delta\boldsymbol{\Omega} = [\boldsymbol{\Gamma}(\boldsymbol{\phi}) \cdot \delta\boldsymbol{\phi}\,] \times \mathbf{1}, \qquad \delta\boldsymbol{\Theta} = [\boldsymbol{\Gamma}^T(\boldsymbol{\phi}) \cdot \delta\boldsymbol{\phi}\,] \times \mathbf{1}, \tag{2.24}$$

where

$$\boldsymbol{\Gamma}(\boldsymbol{\phi}) = \mathbf{1} + \frac{1-\cos\phi}{\phi^2}\,\boldsymbol{\phi} \times \mathbf{1} + \frac{1}{\phi^2}(1 - \frac{\sin\phi}{\phi})\,\boldsymbol{\phi} \times (\boldsymbol{\phi} \times \mathbf{1}). \tag{2.25}$$

Note that the weak forms (2.18) and (2.21) can also be derived from the two-field dual-mixed variational principle of Fraeijs de Veubeke [28].

2.5. **Linearization.** To linearize the weak forms of the kinematic equation and the angular momentum balance equation, (2.18) and (2.21), their directional derivatives should be computed in the independent variable directions $\Delta\boldsymbol{P}$ and $\Delta\boldsymbol{R}$, which represent sufficiently small increments in the stress- and rotation tensors. Assuming that the rotation tensor $\boldsymbol{R}$ is parameterized with respect to the rotation vector $\boldsymbol{\phi}$, according to (2.23), the directional derivative of $\boldsymbol{R} = \boldsymbol{R}(\boldsymbol{\phi})$ at $\boldsymbol{\phi}$ in the direction of the vectorial rotation increment $\Delta\boldsymbol{\phi}$ can be computed as

$$\Delta\boldsymbol{R} = D\boldsymbol{R}(\boldsymbol{\phi})[\Delta\boldsymbol{\phi}] = \boldsymbol{R} \cdot \Delta\boldsymbol{\Theta}, \qquad \Delta\boldsymbol{\Theta} = [\boldsymbol{\Gamma}^T(\boldsymbol{\phi}) \cdot \Delta\boldsymbol{\phi}\,] \times \mathbf{1}, \tag{2.26}$$

where the tangent tensor $\boldsymbol{\Gamma}(\boldsymbol{\phi})$ is given by (2.25).

2.5.1. *Directional derivatives of $\boldsymbol{T}$ and $\boldsymbol{U}$.* In the present formulation the Biot stress tensor

$$\boldsymbol{T}(\boldsymbol{P}, \boldsymbol{R}) = \boldsymbol{R}^T \cdot \boldsymbol{P}, \tag{2.27}$$

introduced in (2.8), depends on both $\boldsymbol{P}$ and $\boldsymbol{R}$. The directional derivatives of $\boldsymbol{T}$ at $\boldsymbol{P}$ and $\boldsymbol{R}$ in the directions of $\Delta\boldsymbol{P}$ and $\Delta\boldsymbol{R}$ can be written as

$$\Delta\boldsymbol{T} = \Delta_{\boldsymbol{P}}\boldsymbol{T} + \Delta_{\boldsymbol{R}}\boldsymbol{T}, \tag{2.28}$$

where, in view of (2.27) and (2.26),

$$\Delta_{\boldsymbol{P}}\boldsymbol{T} \equiv D\,\boldsymbol{T}[\Delta\boldsymbol{P}] = \frac{\partial\boldsymbol{T}}{\partial\boldsymbol{P}} : \Delta\boldsymbol{P} = \boldsymbol{R}^T \cdot \Delta\boldsymbol{P}, \tag{2.29}$$

and

$$\Delta_{\boldsymbol{R}}\boldsymbol{T} \equiv D\,\boldsymbol{T}[\Delta\boldsymbol{R}] = \frac{\partial\boldsymbol{T}}{\partial\boldsymbol{R}} : \Delta\boldsymbol{R} = \Delta\boldsymbol{\Theta}^T \cdot \boldsymbol{T}. \tag{2.30}$$

The directional derivative of the right stretch tensor $\boldsymbol{U}(\boldsymbol{T}) = \boldsymbol{U}[\boldsymbol{T}(\boldsymbol{P}, \boldsymbol{R})]$ at $\boldsymbol{P}$ and $\boldsymbol{R}$ in the directions of $\Delta\boldsymbol{P}$ and $\Delta\boldsymbol{R}$ can be computed as

$$\Delta\boldsymbol{U} = \Delta_{\boldsymbol{P}}\boldsymbol{U} + \Delta_{\boldsymbol{R}}\boldsymbol{U}, \tag{2.31}$$

where, taking into account (2.28)-(2.30) and (2.13),

$$\Delta_{\boldsymbol{P}}\boldsymbol{U} \equiv D\,\boldsymbol{U}(\boldsymbol{T})[\Delta\boldsymbol{P}] = \frac{\partial \boldsymbol{U}}{\partial \boldsymbol{T}} : D\,\boldsymbol{T}[\Delta\boldsymbol{P}] = \mathbb{C}^{-1} : \Delta_{\boldsymbol{P}}\boldsymbol{T}, \tag{2.32}$$

$$\Delta_{\boldsymbol{R}}\boldsymbol{U} \equiv D\,\boldsymbol{U}(\boldsymbol{T})[\Delta\boldsymbol{R}] = \frac{\partial \boldsymbol{U}}{\partial \boldsymbol{T}} : D\,\boldsymbol{T}[\Delta\boldsymbol{R}] = \mathbb{C}^{-1} : \Delta_{\boldsymbol{R}}\boldsymbol{T}. \tag{2.33}$$

Then, in view of (2.28), equation (2.31) can be written as

$$\Delta\boldsymbol{U} = \mathbb{C}^{-1} : (\Delta_{\boldsymbol{P}}\boldsymbol{T} + \Delta_{\boldsymbol{R}}\boldsymbol{T}) = \mathbb{C}^{-1} : \Delta\boldsymbol{T}. \tag{2.34}$$

2.5.2. *Directional derivatives of $\delta\mathcal{W}_{\kappa}$ and $\delta\mathcal{W}_{\mathcal{S}}$.* Taking into account (2.26) and (2.32)–(2.33), the directional derivatives of $\delta\mathcal{W}_{\kappa}$ in (2.18) at $\boldsymbol{P}$ and $\boldsymbol{R}$ in the directions of $\Delta\boldsymbol{P}$ and $\Delta\boldsymbol{R}$ are

$$D_{\Delta\boldsymbol{P}}\,\delta\mathcal{W}_{\kappa} = \int_{{}^0V} \delta\boldsymbol{P} : \big\{\boldsymbol{R}\cdot D\,\boldsymbol{U}(\boldsymbol{T})[\Delta\boldsymbol{P}]\big\}\,\mathrm{d}\,{}^0V = \int_{{}^0V} \delta_{\boldsymbol{P}}\boldsymbol{T} : \mathbb{C}^{-1} : \Delta_{\boldsymbol{P}}\boldsymbol{T}\,\mathrm{d}\,{}^0V, \tag{2.35}$$

$$\begin{aligned} D_{\Delta\boldsymbol{R}}\,\delta\mathcal{W}_{\kappa} &= \int_{{}^0V} \delta\boldsymbol{P} : \big\{\Delta\boldsymbol{R}\cdot\boldsymbol{U} + \boldsymbol{R}\cdot D\,\boldsymbol{U}(\boldsymbol{T})[\Delta\boldsymbol{R}]\big\}\,\mathrm{d}\,{}^0V \\ &= \int_{{}^0V} \big[\,\delta_{\boldsymbol{P}}\boldsymbol{T} : (\Delta\boldsymbol{\Theta}\cdot\boldsymbol{U}) + \delta_{\boldsymbol{P}}\boldsymbol{T} : \mathbb{C}^{-1} : \Delta_{\boldsymbol{R}}\boldsymbol{T}\,\big]\,\mathrm{d}\,{}^0V, \end{aligned} \tag{2.36}$$

where

$$\delta_{\boldsymbol{P}}\boldsymbol{T} \equiv D\,\boldsymbol{T}(\boldsymbol{P},\boldsymbol{R})[\delta\boldsymbol{P}] = \frac{\partial \boldsymbol{T}}{\partial \boldsymbol{P}} : \delta\boldsymbol{P} = \boldsymbol{R}^T\cdot\delta\boldsymbol{P}. \tag{2.37}$$

Taking into account (2.26) and (2.29)–(2.30), as well as (2.32)–(2.33), the directional derivatives of $\delta\mathcal{W}_{\mathcal{S}}$ in (2.21) at $\boldsymbol{P}$ and $\boldsymbol{R}$ in the directions of $\Delta\boldsymbol{P}$ and $\Delta\boldsymbol{R}$ are

$$\begin{aligned} D_{\Delta\boldsymbol{P}}\,\delta\mathcal{W}_{\mathcal{S}} &= \int_{{}^0V} \delta\boldsymbol{\Theta} : \big\{D\,\boldsymbol{T}[\Delta\boldsymbol{P}]\cdot\boldsymbol{U} + \boldsymbol{T}\cdot D\,\boldsymbol{U}(\boldsymbol{T})[\Delta\boldsymbol{P}]\big\}\,\mathrm{d}\,{}^0V \\ &= \int_{{}^0V} \big[\,(\delta\boldsymbol{\Theta}\cdot\boldsymbol{U}) : \Delta_{\boldsymbol{P}}\boldsymbol{T} + \delta_{\boldsymbol{R}}\boldsymbol{T} : \mathbb{C}^{-1} : \Delta_{\boldsymbol{P}}\boldsymbol{T}\,\big]\,\mathrm{d}\,{}^0V, \end{aligned} \tag{2.38}$$

$$\begin{aligned} D_{\Delta\boldsymbol{R}}\,\delta\mathcal{W}_{\mathcal{S}} &= \int_{{}^0V} \delta\boldsymbol{\Theta} : \big\{D\,\boldsymbol{T}[\Delta\boldsymbol{R}]\cdot\boldsymbol{U} + \boldsymbol{T}\cdot D\,\boldsymbol{U}(\boldsymbol{T})[\Delta\boldsymbol{R}]\big\}\,\mathrm{d}\,{}^0V \\ &= \int_{{}^0V} \big[\,(\boldsymbol{T}\cdot\boldsymbol{U}) : (\delta\boldsymbol{\Theta}\cdot\Delta\boldsymbol{\Theta}) + \delta_{\boldsymbol{R}}\boldsymbol{T} : \mathbb{C}^{-1} : \Delta_{\boldsymbol{R}}\boldsymbol{T}\,\big]\,\mathrm{d}\,{}^0V, \end{aligned} \tag{2.39}$$

where

$$\delta_{\boldsymbol{R}}\boldsymbol{T} \equiv D\,\boldsymbol{T}(\boldsymbol{P},\boldsymbol{R})[\delta\boldsymbol{R}] = \frac{\partial \boldsymbol{T}}{\partial \boldsymbol{R}} : \delta\boldsymbol{R} = \delta\boldsymbol{\Theta}^T\cdot\boldsymbol{T}. \tag{2.40}$$

2.5.3. *Linearized weak forms.* Considering a trial solution ${}^t\boldsymbol{P}$ and ${}^t\boldsymbol{R}$, the weak forms of the kinematic equation (2.18) and the angular momentum balance equation (2.21) can be linearized in the directions of the stress- and rotation increments $\Delta\boldsymbol{P}$ and $\Delta\boldsymbol{R}$ at ${}^t\boldsymbol{P}$ and ${}^t\boldsymbol{R}$ according to

$$\delta\mathcal{W}_{\kappa}({}^t\boldsymbol{P},{}^t\boldsymbol{R},\delta\boldsymbol{P}) + D_{\Delta\boldsymbol{P}}\,\delta\mathcal{W}_{\kappa}({}^t\boldsymbol{P},{}^t\boldsymbol{R},\delta\boldsymbol{P}) + D_{\Delta\boldsymbol{R}}\,\delta\mathcal{W}_{\kappa}({}^t\boldsymbol{P},{}^t\boldsymbol{R},\delta\boldsymbol{P}) = 0, \tag{2.41}$$

$$\delta\mathcal{W}_{\mathcal{S}}({}^t\boldsymbol{P},{}^t\boldsymbol{R},\delta\boldsymbol{R}) + D_{\Delta\boldsymbol{P}}\,\delta\mathcal{W}_{\mathcal{S}}({}^t\boldsymbol{P},{}^t\boldsymbol{R},\delta\boldsymbol{R}) + D_{\Delta\boldsymbol{R}}\,\delta\mathcal{W}_{\mathcal{S}}({}^t\boldsymbol{P},{}^t\boldsymbol{R},\delta\boldsymbol{R}) = 0. \tag{2.42}$$

Taking into account (2.35)–(2.36) and (2.38)–(2.39), equations (2.41) and (2.42) can be written as

$$\int_{{}^0V} \big[\, \delta_{\boldsymbol{P}}\boldsymbol{T} :\, {}^t\mathbb{C}^{-1} : \Delta\boldsymbol{T} \;+\; \delta_{\boldsymbol{P}}\boldsymbol{T} : (\Delta\boldsymbol{\Theta} \cdot {}^t\boldsymbol{U})\big]\, \mathrm{d}\, {}^0V + \int_{{}^0V} \delta\boldsymbol{P} : ({}^t\boldsymbol{R} \cdot {}^t\boldsymbol{U} - \mathbf{1})\, \mathrm{d}\, {}^0V - \int_{{}^0S_u} \widetilde{\boldsymbol{u}} \cdot \delta\boldsymbol{P} \cdot {}^0\boldsymbol{n}\, \mathrm{d}\, {}^0S = 0, \tag{2.43}$$

$$\int_{{}^0V} \big[\, \delta_{\boldsymbol{R}}\boldsymbol{T} :\, {}^t\mathbb{C}^{-1} : \Delta\boldsymbol{T} \;+\; \Delta_{\boldsymbol{P}}\boldsymbol{T} : (\delta\boldsymbol{\Theta} \cdot {}^t\boldsymbol{U}) + ({}^t\boldsymbol{T} \cdot {}^t\boldsymbol{U}) : (\delta\boldsymbol{\Theta} \cdot \Delta\boldsymbol{\Theta})\big]\, \mathrm{d}\, {}^0V + \int_{{}^0V} \delta\boldsymbol{\Theta} : ({}^t\boldsymbol{T} \cdot {}^t\boldsymbol{U})\, \mathrm{d}\, {}^0V = 0, \tag{2.44}$$

where ${}^t\mathbb{C}^{-1}$ is the tangent compliance tensor at ${}^t\boldsymbol{T} = {}^t\boldsymbol{R}^T \cdot {}^t\boldsymbol{P}$. The linearized weak forms (2.43) and (2.44) serve as the basis for the dual-mixed finite element solution procedure of the nonlinear elasticity problem. Note that when the approximation is based on the Bubnov-Galerkin method, the above dual-mixed formulation leads to symmetric system matrices.

Subsidiary conditions to the weak forms (2.43)–(2.44), to be *a priori* satisfied during the incremental solution procedure, are the translational equilibrium equation

$$\Delta\boldsymbol{P} \cdot {}^0\nabla + {}^0\rho\boldsymbol{b} = \mathbf{0}, \qquad {}^0\boldsymbol{x} \in {}^0V, \tag{2.45}$$

and the stress boundary condition

$$\Delta\boldsymbol{P} \cdot {}^0\boldsymbol{n} = {}^0\widetilde{\boldsymbol{p}}\,, \qquad {}^0\boldsymbol{x} \in {}^0S_p\,. \tag{2.46}$$

At the initial, stress-free configuration the trial solution in (2.43)–(2.44) is ${}^t\boldsymbol{P} = \mathbf{0}$ and ${}^t\boldsymbol{R} = \mathbf{1}$ from which it follows that ${}^t\boldsymbol{T} = {}^t\boldsymbol{R}^T \cdot {}^t\boldsymbol{P} = \mathbf{0}$ and

$$\delta_{\boldsymbol{R}}\boldsymbol{T} = \Delta_{\boldsymbol{R}}\boldsymbol{T} = \mathbf{0}, \qquad \delta_{\boldsymbol{P}}\boldsymbol{T} = \delta\boldsymbol{P} = \delta\boldsymbol{T}, \qquad \Delta_{\boldsymbol{P}}\boldsymbol{T} = \Delta\boldsymbol{P} = \Delta\boldsymbol{T}. \tag{2.47}$$

Since ${}^t\boldsymbol{U} = \mathbf{1}$ and ${}^t\boldsymbol{\phi} = \mathbf{0}$ also hold, from (2.24)–(2.26) it follows that

$$\delta\boldsymbol{\Theta} = \delta\boldsymbol{\phi} \times \mathbf{1}, \qquad \Delta\boldsymbol{\Theta} = \Delta\boldsymbol{\phi} \times \mathbf{1}, \tag{2.48}$$

and the linearized weak forms (2.43)–(2.44) simplify to

$$\int_{{}^0V} (\, \delta\boldsymbol{T} : \mathbb{C}^{-1} : \Delta\boldsymbol{T} + \delta\boldsymbol{T} : \Delta\boldsymbol{\Theta}\,)\, \mathrm{d}\, {}^0V - \int_{{}^0S_u} \widetilde{\boldsymbol{u}} \cdot \delta\boldsymbol{T} \cdot {}^0\boldsymbol{n}\, \mathrm{d}\, {}^0S = 0, \tag{2.49}$$

$$\int_{{}^0V} \delta\boldsymbol{\Theta} : \Delta\boldsymbol{T}\, \mathrm{d}\, {}^0V = 0. \tag{2.50}$$

Finite element models based on the above weak forms requires *a priori* satisfaction of the subsidiary conditions (2.45)–(2.46) and leads to a stress-based numerical solution of the linear elasticity problem. The translational equilibrium equation (2.45) can identically be satisfied by introducing first-order stress functions [15, 29]. The stress boundary condition (2.46) is usually taken into account in the course of the finite element solution procedure by applying hybridization techniques [13, 18].

## 3. Dimensional reduction for plates in terms of stresses

This section presents a stress-based dimensional reduction procedure for linearly elastic plates. The independent variables, the non-symmetric stresses and the rotations, are expanded into power series with respect to the thickness coordinate. After making assumptions on the transverse variations of the stress components across the thickness, the translational equilibrium equations will be satisfied by introducing one first-order stress function vector. The stress boundary conditions on the faces of the plate are incorporated into the equilibrated stress space. The weak formulation for the plate model, which serve as a basis for the development of the dual-mixed *hp* finite elements in Sections 4 and 5, will be derived from the linearized three-dimensional weak forms (2.49) and (2.50).

3.1. **Notation for plates.** In the developments of this section, the index notation of tensor variables is used. The left superscript 0, referring to the initial configuration, will be neglected for $\boldsymbol{x}$, $\boldsymbol{n}$, $\boldsymbol{p}$, $\rho$, $V$, $S$ and $\nabla$, as notational distinction between the reference and the current configuration is unnecessary in the linear elastic case.

The reference configuration of the three-dimensional plate of thickness $d$ is denoted by

$$V = \{x_a \in \mathbb{R}^3 : x_\alpha \in \bar{S},\ |x_3| < d/2\}, \tag{3.1}$$

where $\bar{S} \in \mathbb{R}^2$ is the reference middle plane of the plate, parameterized by the Cartesian coordinates $x_\alpha$, and the coordinate $x_3$ is measured along a straight line perpendicular to $\bar{S}$. It is assumed that both $V$ and $\bar{S}$ are simply connected and bounded sets in $\mathbb{R}^3$ and $\mathbb{R}^2$, respectively, and the thickness $d$ is independent of $x_\alpha$.

The boundary of $V$, denoted by $S$, consists of the top and bottom surfaces $S^\pm$ and the lateral surface $S^\times$ ($S = S^\pm \cup S^\times$, $S^\pm \cap S^\times = \emptyset$) with outward unit normals $\boldsymbol{n}^\pm = \pm\boldsymbol{e}_3$ and $\boldsymbol{n}^\times = n^\times_\lambda \boldsymbol{e}_\lambda$, respectively. It is assumed that the plate is subjected to body forces $\rho\boldsymbol{b}$ in $V$ and surface loads $\widetilde{\boldsymbol{p}}^{\,\pm}$ on $S^\pm$. On the lateral surface $S^\times = S^\times_p \cup S^\times_u$ ($S^\times_p \cap S^\times_u = \emptyset$), surface load $\widetilde{\boldsymbol{p}}^{\,\times}$ on $S^\times_p$ and the displacement vector $\widetilde{\boldsymbol{u}}^{\,\times}$ on $S^\times_u$ are prescribed. The boundary curve of the reference middle plane, $\bar{S}$, is denoted by $\ell = \ell_u \cup \ell_p$ ($\ell_u \cap \ell_p = \emptyset$).

3.2. **Approximation of the stress space across the thickness.** Applying index notation, the linearized weak forms (2.49)–(2.50) can be written as

$$\int_V \left( \delta T_{ij}\, \mathbb{C}^{-1}_{ijk\ell}\, T_{k\ell} + \delta T_{k\ell}\, \Theta_{k\ell} \right) \mathrm{d}V - \int_{S^\times_u} \widetilde{u}^\times_k\, \delta T_{k\lambda}\, n^\times_\lambda \, \mathrm{d}S = 0, \tag{3.2}$$

$$\int_V \delta\Theta_{k\ell}\, T_{k\ell} \, \mathrm{d}V = 0, \tag{3.3}$$

where, for the sake of notational simplicity, the sign $\Delta$ is neglected in the first increment of the stress- and rotation tensors, i.e., $\Delta T_{k\ell} = T_{k\ell}$ and $\Delta\Theta_{k\ell} = \Theta_{k\ell}$ correspond to the linear solution. Assuming linearly elastic and isotropic material,

$$\mathbb{C}^{-1}_{ijk\ell} = \frac{1}{2\mu}\Big[\frac{1}{2}(\delta_{ik}\delta_{j\ell} + \delta_{i\ell}\delta_{jk}) - \frac{\nu}{1+\nu}\,\delta_{ij}\delta_{k\ell}\Big] \tag{3.4}$$

with Kronecker symbol $\delta_{ij}$, shear modulus $\mu$ and Poisson ratio $\nu$. The components of the stress tensor $\boldsymbol{T} = \boldsymbol{p}_\ell\, \boldsymbol{e}_\ell = T_{k\ell}\, \boldsymbol{e}_k \boldsymbol{e}_\ell$ with stress vector $\boldsymbol{p}_\ell$ should *a priori* satisfy the translational equilibrium equations

$$T_{k\ell,\ell} + \rho b_k = 0 \tag{3.5}$$

and the stress boundary conditions on the faces and on the lateral surfaces of the plate:

$$\boldsymbol{T} \cdot \boldsymbol{n}^{\pm} = \pm\, \boldsymbol{p}_3 = \widetilde{\boldsymbol{p}}^{\,\pm} \qquad \text{on } S_p^{\pm}, \tag{3.6}$$

$$\boldsymbol{T} \cdot \boldsymbol{n}^{\times} = n_\lambda^{\times}\, \boldsymbol{p}_\lambda = \widetilde{\boldsymbol{p}}^{\,\times} \qquad \text{on } S_p^{\times}. \tag{3.7}$$

In (3.5), the comma followed by the index $\ell$ in the right subscript denotes partial differentiation with respect to $x_\ell$.

The first step in the derivation of the stress-based, dimensionally reduced plate model is the expansion of the stress components and the prescribed body forces into power series with respect to the thickness coordinate $x_3$, according to

$$T_{k\ell}(x_\alpha, x_3) = \sum_{i=0}^{n} {}_iT_{k\ell}(x_\alpha)\, (x_3)^i, \qquad b_\ell(x_\alpha, x_3) = \sum_{i=0}^{n} {}_ib_\ell(x_\alpha)\, (x_3)^i, \tag{3.8}$$

where $n > 0$ is an integer. According to the notation applied in (3.8), an index on the left subscript refers to the power of $x_3$. Substituting (3.8) into (3.5) and making separation with respect to the powers of $x_3$, we obtain a set of two-dimensional equilibrium equations:

$${}_iT_{k\lambda,\lambda} + (i+1)\, {}_{i+1}T_{k3} + \rho\, {}_ib_k = 0, \quad i = 0, 1, 2, ..., n. \tag{3.9}$$

Depending on the number of $n$ chosen, a variety of plate models can be derived.

The next step in the derivation of the plate model is making assumptions on the transverse variations of the three-dimensional stress components. In this paper, a model described by $n = 1$ in (3.9) is chosen, which means that the first two equilibrium equations of (3.9) are selected:

$${}_0T_{k\lambda,\lambda} + {}_1T_{k3} + \rho\, {}_0b_k = 0, \tag{3.10}$$

$${}_1T_{k\lambda,\lambda} + 2\, {}_2T_{k3} + \rho\, {}_1b_k = 0, \tag{3.11}$$

and the equations characterized by $n > 1$ are neglected with the assumption that they are identically satisfied. Following from (3.10)-(3.11), the transverse variations of the stress components in $x_3$ are assumed to be

$$T_{k\lambda}(x_\alpha, x_3) = {}_0T_{k\lambda}(x_\alpha) + {}_1T_{k\lambda}(x_\alpha)\, x_3, \tag{3.12}$$

$$T_{k3}(x_\alpha, x_3) = {}_0T_{k3}(x_\alpha) + {}_1T_{k3}(x_\alpha)\, x_3 + {}_2T_{k3}(x_\alpha)\, (x_3)^2, \tag{3.13}$$

i.e., the stress vectors $\boldsymbol{p}_\lambda = \boldsymbol{T} \cdot \boldsymbol{e}_\lambda = T_{k\lambda}\, \boldsymbol{e}_k$, parallel to the middle plane of the plate, are linear functions of the coordinate $x_3$, whereas the stress vector $\boldsymbol{p}_3 = \boldsymbol{T} \cdot \boldsymbol{e}_3 = T_{k3}\, \boldsymbol{e}_k$, perpendicular to the middle plane, is parabolic in $x_3$.

To keep the number of the independent stress components as minimal as possible, the stress boundary conditions on the top and bottom faces of the plate will be incorporated in the equilibrium equations (3.10)–(3.11), just like in the case of the stress resultant-based shell models. By the procedure described subsequently, the

number of the independent stress coefficients in (3.12)–(3.13) can be reduced from 21 to 15.

Taking into account (3.13), the stress boundary conditions (3.6) on the top and bottom faces of the plate can be written as

$$ {}_0T_{k3} \pm {}_1T_{k3}\,\frac{d}{2} + {}_2T_{k3}\,\frac{d^2}{4} = \pm\widetilde{p}_k^{\pm} \qquad \text{on } S_p^{\pm}. \tag{3.14} $$

Adding and subtracting the two equations in (3.14) and defining the load vector

$$ \widetilde{\boldsymbol{p}}\,(x_\alpha, x_3) = {}_0\widetilde{\boldsymbol{p}} + {}_1\widetilde{\boldsymbol{p}}\,x^3, \qquad \widetilde{\boldsymbol{p}}\,(x_\alpha, \pm d/2) := \pm\widetilde{\boldsymbol{p}}^{\pm} \tag{3.15} $$

with coefficients

$$ {}_0\widetilde{\boldsymbol{p}}\,(x_\alpha) = \frac{1}{2}\,(\widetilde{\boldsymbol{p}}^{+} - \widetilde{\boldsymbol{p}}^{-}), \qquad {}_1\widetilde{\boldsymbol{p}}\,(x_\alpha) = \frac{1}{d}\,(\widetilde{\boldsymbol{p}}^{+} + \widetilde{\boldsymbol{p}}^{-}), \tag{3.16} $$

the stress boundary conditions (3.14) can be rewritten as

$$ {}_0T_{k3} + \frac{d^2}{4}\,{}_2T_{k3} = {}_0\widetilde{p}_k, \tag{3.17} $$

$$ {}_1T_{k3} = {}_1\widetilde{p}_k. \tag{3.18} $$

Making use of (3.17)–(3.18), the two equilibrium equations in (3.10)–(3.11) take the forms

$$ {}_0T_{k\lambda,\lambda} + {}_1\widetilde{p}_k + \rho\,{}_0b_k = 0, \tag{3.19} $$

$$ {}_1T_{k\lambda,\lambda} - \frac{8}{d^2}\,{}_0T_{k3} + \frac{8}{d^2}\,{}_0\widetilde{p}_k + \rho\,{}_1b_k = 0. \tag{3.20} $$

To obtain a numerically more efficient formulation, the number of the independent stress variables can be further reduced by satisfying the symmetry of the transverse shear stresses in an integral average sense, according to the equation

$$ \int_{-d/2}^{+d/2} T_{\lambda 3}\,\mathrm{d}x_3 = \int_{-d/2}^{+d/2} T_{3\lambda}\,\mathrm{d}x_3. \tag{3.21} $$

Carrying out the integration in (3.21) by taking into account (3.12)–(3.13) and the stress boundary conditions (3.17)–(3.18), the following equations are obtained:

$$ {}_0T_{\lambda 3} = \frac{3}{2}\,{}_0T_{3\lambda} - \frac{1}{2}\,{}_0\widetilde{p}_\lambda, \qquad {}_1T_{\lambda 3} = {}_1T_{3\lambda} = {}_1\widetilde{p}_\lambda. \tag{3.22} $$

Substituting them into (3.20), the three equilibrium equations take the forms

$$ {}_1T_{\kappa\lambda,\lambda} - \frac{12}{d^2}\,{}_0T_{3\kappa} + \frac{12}{d^2}\,{}_0\widetilde{p}_\kappa + \rho\,{}_1b_\kappa = 0, \tag{3.23} $$

$$ {}_0T_{33} = {}_0\widetilde{p}_3 + \frac{d^2}{8}({}_1\widetilde{p}_{\lambda,\lambda} + \rho\,{}_1b_3). \tag{3.24} $$

Equation (3.24) indicates that the transverse normal stress ${}_0T_{33}$ is determined by the prescribed surface and body loads. Since ${}_1T_{33}$ is given by (3.18) and ${}_2T_{33}$ is obtained from (3.17) using (3.24), the parabolic transverse normal stress $T_{33}$ is completely determined by the prescribed surface loads on the top and bottom faces and by the body forces. Thus, the equilibrium of the plate is described by three membrane equilibrium

equations in (3.19) and two bending equilibrium equations in (3.23), written in terms of 10 independent stress coefficients.

3.3. **Equilibrated stress space using first-order stress functions.** The five two-dimensional equilibrium equations in (3.19) and (3.23) can identically be satisfied by introducing one first-order stress function vector

$$\boldsymbol{\psi}(x_\alpha, x_3) = {}_0\boldsymbol{\psi}(x_\alpha) \,+\, {}_1\boldsymbol{\psi}(x_\alpha)\, x_3 = {}_0\psi_\ell(x_\alpha)\, \boldsymbol{e}_\ell \,+\, {}_1\psi_\lambda(x_\alpha)\, x_3\, \boldsymbol{e}_\lambda \tag{3.25}$$

with component-wise transverse variations

$$\psi_\lambda(x_\alpha, x_3) = {}_0\psi_\lambda(x_\alpha) + {}_1\psi_\lambda(x_\alpha)\, x_3\,, \tag{3.26}$$

$$\psi_3(x_\alpha, x_3) = {}_0\psi_3(x_\alpha). \tag{3.27}$$

Applying the five two-dimensional stress function coefficients appearing in (3.26)–(3.27), the three membrane equilibrium equations in (3.19) can be satisfied using stress functions ${}_0\psi_\lambda$ as

$${}_0T_{11} = {}_0\psi_{1,2} - {}_0f_1, \qquad {}_0T_{12} = -\,{}_0\psi_{1,1}, \tag{3.28}$$

$${}_0T_{21} = {}_0\psi_{2,2}, \qquad {}_0T_{22} = -\,{}_0\psi_{2,1} - {}_0f_2, \tag{3.29}$$

where

$${}_0f_\lambda(x_\alpha) = \int_{\xi=0}^{x_\lambda} ({}_1\widetilde{p}_\lambda + \rho\, {}_0b_\lambda)\, \mathrm{d}\xi, \tag{3.30}$$

and the two bending equilibrium equations in (3.23) can be satisfied using stress functions ${}_0\psi_3$ and ${}_1\psi_\lambda$ as

$${}_0T_{31} = {}_0\psi_{3,2} - \frac{1}{2} f_{3,2}, \qquad {}_0T_{32} = -\,{}_0\psi_{3,1} - \frac{1}{2} f_{3,1}, \tag{3.31}$$

$${}_1T_{11} = {}_1\psi_{1,2} - {}_1f_1, \qquad {}_1T_{12} = -\,{}_1\psi_{1,1} + \frac{12}{d^2}\, {}_0\psi_3 - \frac{6}{d^2} f_3, \tag{3.32}$$

$${}_1T_{21} = {}_1\psi_{2,2} - \frac{12}{d^2}\, {}_0\psi_3 - \frac{6}{d^2} f_3, \qquad {}_1T_{22} = -\,{}_1\psi_{2,1} - {}_1f_2, \tag{3.33}$$

where

$${}_1f_\lambda(x_\alpha) = \int_{\xi=0}^{x_\lambda} (\frac{12}{d^2}\, {}_0\widetilde{p}_\lambda + \rho\, {}_1b_\lambda)\, \mathrm{d}\xi, \qquad f_3(x_\alpha) = \int_{\eta=0}^{x_2} \int_{\xi=0}^{x_1} ({}_1\widetilde{p}_3 + \rho\, {}_0b_3)\, \mathrm{d}\xi\, \mathrm{d}\eta. \tag{3.34}$$

Note that the stress coefficients ${}_iT_{k3},\ i = 0, 1, 2$, appearing in the truncated power series (3.13), are determined by equations (3.17)–(3.18), (3.22) and (3.24), i.e., by the surface and body loads and the stress coefficients in (3.31). According to equations (3.28)–(3.29) and (3.31)–(3.33), the equilibrium of the plate in terms of 10 independent stress coefficients can be satisfied by 5 first-order stress functions.

3.4. **Approximation of the rotation vector across the thickness.** Considering the equilibrated stress space given in Subsection 3.3 in terms of first-order stress functions, the only symmetry condition remaining to be satisfied is the symmetry of the shear stresses $T_{12} = T_{21}$. This constraint is enforced weakly through functional (3.3) by considering the rotation component $\phi_3 = \Theta_{21}$ as an independent variable. Since the shear stresses $T_{12}$ and $T_{21}$ are approximated by linear polynomials in $x_3$,

according to (3.12), the corresponding Lagrange multiplier, i.e., the rotation $\phi_3$, is approximated by linear polynomial as well through the thickness:

$$\phi_3(x_\alpha, x_3) \;=\; {}_0\phi_3(x_\alpha) \;+\; {}_1\phi_3(x_\alpha)\, x_3. \tag{3.35}$$

The symmetry of the in-plane shear stresses ${}_0T_{12} = {}_0T_{21}$ will be enforced by ${}_0\phi_3$, and that of the torsional stresses ${}_1T_{12} = {}_1T_{21}$ by ${}_1\phi_3$. Note that the rotation around the normal to the middle surface has also been approximated by a linear function across the thickness in [30], though in a different theoretical setting.

3.5. **Weak forms of the plate model with first-order stress functions and rotations.** The weak forms of the stress-based dimensionally reduced plate model in terms of first-order stress functions and rotations can be obtained from the three-dimensional weak forms (3.2)–(3.3) by carrying out the following steps. First, the expanded stress and rotation components (3.12)–(3.13) and (3.35), as well as the elastic compliance tensor (3.4), should be inserted in (3.2)–(3.3). Note that using $\mathbb{C}^{-1}_{ijk\ell}$ in (3.2) means that this plate model relies on unmodified three-dimensional constitutive equations. In the second step, relations (3.17)–(3.18), (3.22) and (3.24), as well as (3.28)–(3.29) and (3.31)–(3.33) should be inserted in the weak forms. Finally, by carrying out all the integrations with respect to the thickness coordinate $x_3$, as a third step, the following 2D weak forms of the kinematic equation and the angular momentum balance are obtained from (3.2)–(3.3):

$$\mathscr{A}(\delta\boldsymbol{\psi}, \boldsymbol{\psi}) + \mathscr{B}(\delta\boldsymbol{\psi}, \boldsymbol{\phi}) = \mathscr{P}(\delta\boldsymbol{\psi}, \widetilde{\boldsymbol{p}}) + \mathscr{U}(\delta\boldsymbol{\psi}, \widetilde{\boldsymbol{u}}), \tag{3.36}$$

$$\mathscr{B}(\delta\boldsymbol{\phi}, \boldsymbol{\psi}) \;=\; 0, \tag{3.37}$$

where the bilinear forms $\mathscr{A}(\delta\boldsymbol{\psi}, \boldsymbol{\psi})$ and $\mathscr{B}(\delta\boldsymbol{\phi}, \boldsymbol{\psi})$ and the linear forms $\mathscr{P}(\delta\boldsymbol{\psi}, \widetilde{\boldsymbol{p}})$ and $\mathscr{U}(\delta\boldsymbol{\psi}, \widetilde{\boldsymbol{u}})$ are detailed subsequently. An important observation is that each of the above bilinear and linear forms can be divided into a membrane part, a shear part, and a bending part. The bilinear form $\mathscr{A}(\delta\boldsymbol{\psi}, \boldsymbol{\psi})$ in (3.36) can be written as

$$\mathscr{A}(\delta\boldsymbol{\psi}, \boldsymbol{\psi}) = \mathscr{A}_m(\delta_0\psi_\lambda,\, {}_0\psi_\lambda) + \mathscr{A}_s(\delta_0\psi_3,\, {}_0\psi_3) + \mathscr{A}_b(\delta_1\psi_\lambda,\, {}_1\psi_\lambda), \tag{3.38}$$

where the membrane, shear and bending parts are given, respectively, by

$$\begin{aligned}\mathscr{A}_m(\delta_0\psi_\lambda,\, {}_0\psi_\lambda) = d\int_{\bar S}\big[\frac{1}{E}\big(\,&\delta_0\psi_{1,2}\,{}_0\psi_{1,2} + \delta_0\psi_{2,1}\,{}_0\psi_{2,1} + \nu\,\delta_0\psi_{1,2}\,{}_0\psi_{2,1} + \nu\,\delta_0\psi_{2,1}\,{}_0\psi_{1,2}\big)\\ &+\;\frac{1}{4\mu}\big(\delta_0\psi_{1,1}\,{}_0\psi_{1,1} + \delta_0\psi_{2,2}\,{}_0\psi_{2,2} - \delta_0\psi_{1,1}\,{}_0\psi_{2,2} - \delta_0\psi_{2,2}\,{}_0\psi_{1,1}\big)\big]\,\mathrm{d}\bar S,\end{aligned} \tag{3.39}$$

$$\mathscr{A}_s(\delta_0\psi_3,\, {}_0\psi_3) \;=\; \frac{21d}{20\mu}\int_{\bar S}\big(\,\delta_0\psi_{3,1}\,{}_0\psi_{3,1} + \delta_0\psi_{3,2}\,{}_0\psi_{3,2}\big)\,\mathrm{d}\bar S, \tag{3.40}$$

$$\begin{aligned}\mathscr{A}_b(\delta_1\psi_\lambda,\, {}_1\psi_\lambda) = \frac{d^3}{12}\int_{\bar S}\big[\frac{1}{E}\big(\,&\delta_1\psi_{1,2}\,{}_1\psi_{1,2} + \delta_1\psi_{2,1}\,{}_1\psi_{2,1} + \nu\,\delta_1\psi_{1,2}\,{}_1\psi_{2,1} + \nu\,\delta_1\psi_{2,1}\,{}_1\psi_{1,2}\big)\\ &+\;\frac{1}{4\mu}\big(\delta_1\psi_{1,1}\,{}_1\psi_{1,1} + \delta_1\psi_{2,2}\,{}_1\psi_{2,2} - \delta_1\psi_{1,1}\,{}_1\psi_{2,2} - \delta_1\psi_{2,2}\,{}_1\psi_{1,1}\big)\big]\,\mathrm{d}\bar S,\end{aligned} \tag{3.41}$$

with elasticity modulus $E = 2\mu(1+\nu)$. Note that the membrane part depends on stress functions ${}_0\psi_\lambda$, the shear part on ${}_0\psi_3$, and the bending part on ${}_1\psi_\lambda$; i.e., the three parts, expressing the complementary virtual work of the inner forces in the plate, are uncoupled.

The bilinear form $\mathscr{B}(\delta\boldsymbol{\phi},\boldsymbol{\psi})$ in (3.36) and (3.37) can be written as

$$\mathscr{B}(\delta\boldsymbol{\phi},\boldsymbol{\psi}) = \mathscr{B}_m(\delta_0\phi_3,\, {}_0\psi_\lambda) + \mathscr{B}_s(\delta_1\phi_3,\, {}_0\psi_3) + \mathscr{B}_b(\delta_1\phi_3,\, {}_1\psi_\lambda), \tag{3.42}$$

where the membrane, shear and bending parts are given, respectively, by

$$\mathscr{B}_m(\delta_0\phi_3,\, {}_0\psi_\lambda) = d\int_{\bar S} \delta_0\phi_3\,({}_0\psi_{1,1} + {}_0\psi_{2,2})\,\mathrm{d}\bar S, \tag{3.43}$$

$$\mathscr{B}_s(\delta_1\phi_3,\, {}_0\psi_3) = -\frac{24}{d^3}\int_{\bar S} \delta_1\phi_3\, {}_0\psi_3\,\mathrm{d}\bar S, \tag{3.44}$$

$$\mathscr{B}_b(\delta_1\phi_3,\, {}_1\psi_\lambda) = \frac{d^3}{12}\int_{\bar S} \delta_1\phi_3\,({}_1\psi_{1,1} + {}_1\psi_{2,2})\,\mathrm{d}\bar S. \tag{3.45}$$

Note that the membrane part depends on stress functions ${}_0\psi_\lambda$ and rotation ${}_0\phi_3$, the shear part on ${}_0\psi_3$ and ${}_1\phi_3$, and the bending part on ${}_1\psi_\lambda$ and and ${}_1\phi_3$. The membrane part is uncoupled from the other two, the shear and bending parts are coupled by the rotation ${}_1\phi_3$, but not by the stress functions.

The right-hand side of the equation (3.36) contains the prescribed loads on the top and bottom faces $S^\pm$ and the prescribed displacements on the lateral surface $S^\times$. The linear form $\mathscr{P}(\delta\boldsymbol{\psi},\widetilde{\boldsymbol{p}})$ can be written as

$$\mathscr{P}(\delta\boldsymbol{\psi},\widetilde{\boldsymbol{p}}) = \mathscr{P}_m(\delta_0\psi_\lambda,\widetilde{\boldsymbol{p}}) + \mathscr{P}_s(\delta_0\psi_3,\widetilde{\boldsymbol{p}}) + \mathscr{P}_b(\delta_1\psi_\lambda,\widetilde{\boldsymbol{p}}), \tag{3.46}$$

where the membrane, shear and bending parts are given, respectively, by

$$\mathscr{P}_m(\delta_0\psi_\lambda,\widetilde{\boldsymbol{p}}) = \int_{\bar S}\frac{d\nu}{E}\,(\delta_0\psi_{1,2} - \delta_0\psi_{2,1})\,{}_0\widetilde{p}_3\,\mathrm{d}\bar S, \tag{3.47}$$

$$\mathscr{P}_s(\delta_0\psi_3,\widetilde{\boldsymbol{p}}) = \int_{\bar S}\frac{21d}{40\mu}\,(\delta\,{}_0\psi_{3,2}\,f_{3,2} - \delta\,{}_0\psi_{3,1}\,f_{3,1})\,\mathrm{d}\bar S, \tag{3.48}$$

$$\mathscr{P}_b(\delta_1\psi_\lambda,\widetilde{\boldsymbol{p}}) = \int_{\bar S}\frac{d^3\nu}{12E}\,(\delta_1\psi_{1,2} - \delta_1\psi_{2,1})\,{}_1\widetilde{p}_3 + \frac{d}{4\mu}\,(\delta_1\psi_{2,2} - \delta_1\psi_{1,1})f_3\,\mathrm{d}\bar S. \tag{3.49}$$

For more algebraic simplicity, the body forces and the tangential loads to the top and bottom faces are neglected in $\mathscr{P}(\delta\boldsymbol{\psi},\widetilde{\boldsymbol{p}})$. The linear form $\mathscr{U}(\delta\boldsymbol{\psi},\widetilde{\boldsymbol{u}})$ can be written as

$$\begin{aligned}\mathscr{U}(\delta\boldsymbol{\psi},\widetilde{\boldsymbol{u}}) &= \mathscr{U}_m(\delta_0\psi_\kappa,\widetilde{\boldsymbol{u}}) + \mathscr{U}_s(\delta_0\psi_3,\widetilde{\boldsymbol{u}}) + \mathscr{U}_b(\delta_1\psi_\kappa,\widetilde{\boldsymbol{u}})\\ &= \int_{\ell_u}\frac{\mathrm{d}(\delta_0\psi_\kappa)}{\mathrm{d}s}\,{}_0\widetilde{U}_\kappa\,\mathrm{d}s - \frac{12}{d^2}\int_{\ell_u}\delta_0\psi_3\,{}_1\widetilde{U}_T\,\mathrm{d}s + \int_{\ell_u}\frac{\mathrm{d}(\delta_1\psi_\kappa)}{\mathrm{d}s}\,{}_1\widetilde{U}_\kappa\,\mathrm{d}s,\end{aligned} \tag{3.50}$$

where

$${}_0\widetilde{U}_\kappa(x_\alpha) = \int_{-d/2}^{+d/2}\widetilde{u}_\kappa^\times\,\mathrm{d}x_3 = d\,{}_0\widetilde{u}_\kappa, \tag{3.51}$$

$${}_1\widetilde{U}_T(x_\alpha) = \int_{-d/2}^{+d/2}x_3\,\widetilde{\boldsymbol{u}}^\times\cdot(\boldsymbol{e}_z\times\boldsymbol{n}^\times)\,\mathrm{d}x_3 = \frac{d^3}{12}\,{}_1\widetilde{u}_T, \tag{3.52}$$

$$ {}_1\widetilde{U}_\kappa(x_\alpha) = \int_{-d/2}^{+d/2} x_3 \, \widetilde{u}_\kappa^\times \, \mathrm{d}x_3 = \frac{d^3}{12} \, {}_1\widetilde{u}_\kappa, \tag{3.53} $$

and ${}_1\widetilde{u}_T$ is the tangential component of the prescribed displacement vector ${}_1\widetilde{\boldsymbol{u}}$ on the lateral surface $S^\times$. Note that the membrane parts of the linear forms $\mathscr{P}(\delta\boldsymbol{\psi}, \widetilde{\boldsymbol{p}})$ and $\mathscr{U}(\delta\boldsymbol{\psi}, \widetilde{\boldsymbol{u}})$ depend on stress functions ${}_0\psi_\lambda$, the shear parts on ${}_0\psi_3$, and the bending parts on ${}_1\psi_\lambda$; i.e., the three parts, expressing the virtual work of the prescribed loads and displacements, are uncoupled, just like the bilinear forms (3.39)–(3.41).

## 4. Finite element formulation

The dual-mixed finite element formulation for the dimensionally reduced plate model, described in Section 3, is based on the the two-dimensional weak forms of the kinematic equation and the angular momentum balance equation, (3.36) and (3.37). The finite element model requires the approximation of five stress functions and two rotations. However, as pointed out in Subsection 3.5, the membrane problem can be treated and solved separately from the bending-shearing problem of the plate, just like in the case of the linear displacement-based models. The membrane model relies on the bilinear forms $\mathscr{A}_m$, $\mathscr{B}_m$ and the linear forms $\mathscr{P}_m$, $\mathscr{U}_m$, detailed in (3.39), (3.43) and (3.47), (3.50), respectively, and requires the approximation of three variables: the stress functions ${}_0\psi_\lambda$ and the rotation ${}_0\phi_3$. The bending model relies on the bilinear forms $\mathscr{A}_s$, $\mathscr{A}_b$, $\mathscr{B}_s$, $\mathscr{B}_b$, and the linear forms $\mathscr{P}_s$, $\mathscr{P}_m$, $\mathscr{U}_s$, $\mathscr{U}_b$, detailed in (3.40)–(3.41), (3.44)–(3.45) and (3.48)–(3.50), respectively, and requires the approximation of four variables: the stress functions ${}_0\psi_3$, ${}_1\psi_\lambda$ and the rotation ${}_1\phi_3$.

The subsequent developments concentrate on the finite element model and solution of the plate bending problem, as the membrane formulation and element have already been developed and presented in [19]. Stable approximation spaces for the variables ${}_1\psi_\lambda$ and ${}_1\phi_3$ can be chosen by utilizing the fact that $\mathscr{A}_b$, $\mathscr{B}_b$ and $\mathscr{U}_b$ in terms of ${}_1\psi_\lambda$ and ${}_1\phi_3$ have the same structure as $\mathscr{A}_m$, $\mathscr{B}_m$ and $\mathscr{U}_m$ in terms of ${}_0\psi_\lambda$ and ${}_0\phi_3$. The stable approximation spaces for the membrane problem in [19] have been chosen by exploiting the analogy between the weak forms of the membrane model and the displacement-pressure formulation of elasticity (or the velocity-pressure formulation of Stokes flow), for which stable approximation spaces have been developed in [31]. From the three sets of approximation spaces investigated and tested in [19] for the membrane problem, the optimal space denoted by DMX-3 is applied here for the variables ${}_1\psi_\lambda$ and ${}_1\phi_3$. The choice of the approximation spaces for the stress function ${}_0\psi_3$ is governed by the weak forms (3.44)–(3.45).

For the finite element solution of the plate problem, we consider a mesh on $\bar{S}$ that consists of convex disjoint quadrilateral elements. One element in the mesh is denoted by $e$. The master element $\hat{e} := \{\xi, \eta : -1 \leq \xi, \eta \leq 1\}$ is a square on the reference plane. We assume a smooth mapping from $\hat{e}$ to $e$. To introduce the approximation spaces for the element variables, let $P_p(\xi, \eta)$ denote the set of polynomials of total degree $p$ on $\hat{e}$, and let $Q_p(\xi, \eta)$ denote the set of polynomials of degree $p$ in each variable. The *hp* dual-mixed plate bending element is based on the following approximation spaces

for $p \geq 2$:

$$
\begin{aligned}
{}_i\psi_\lambda(\xi,\eta) &\in Q_p(\xi,\eta) \cap P_{p+2}(\xi,\eta), \quad i = 1,2, && (4.1)\\
{}_0\psi_3(\xi,\eta) &\in Q_{p-1}(\xi,\eta) \cap P_{p+1}(\xi,\eta), && (4.2)\\
{}_i\phi_3(\xi,\eta) &\in P_{p-1}(\xi,\eta), \quad i = 1,2. && (4.3)
\end{aligned}
$$

Applying these approximation spaces, a hierarchic sequence of *hp*-version plate bending elements has been developed for $2 \leq p \leq 9$.

The error of the numerical solution in the energy norm is computed using the complementary strain energy of the stress space. A comparable error measure is guaranteed by the fact that the strain energy is equal to the complementary strain energy for a linearly elastic problem. Denoting the analytic solution for the stress space by $\boldsymbol{T}$ and the numerical solution by $\boldsymbol{T}_N$, a monotonically convergent error measure in energy norm is obtained by

$$
\| \boldsymbol{T} - \boldsymbol{T}_N \|_{E(V)} = \Big( \int_V (\boldsymbol{T} - \boldsymbol{T}_N) : \mathbb{C}^{-1} : (\boldsymbol{T} - \boldsymbol{T}_N) \, \mathrm{d}V + \frac{1}{\mu} \int_V (\boldsymbol{T}_N - \boldsymbol{T}_N^T)^2 \, \mathrm{d}V \Big)^{\frac{1}{2}}, \quad (4.4)
$$

where the second term on the right-hand side takes into account the error in the unbalanced symmetry of the computed stress space.

## 5. Numerical results and comparisons

In this section, the approximation capabilities of the seven-field stress-based plate model and the numerical performance of the related dual-mixed *hp* plate bending finite elements, developed and described in Sections 3 and 4, will be presented. The numerical results are obtained using a finite element research code written in the C/C++ programming language. The polynomial space over the elements is spanned by standard hierarchical basis functions based on orthogonal Legendre polynomials [9]. The numerical integrations over the elements have been performed by applying a 14-point Gaussian quadrature rule. The finite element solution is computed for the first-order stress functions and the rotations. The total number of degrees of freedom is obtained as the sum of the stress function and rotational degrees of freedom.

One of the main points of interest in the numerical analysis is the computation of the modeling error of the new plate model with respect to the three-dimensional solution for different thicknesses, and the comparison of the modeling error to those of the classical displacement-based Kirchhoff- and Reissner–Mindlin plate models. The numerical justification of the shear-locking-free property and the incompressibility-locking-free property of the dual-mixed plate element is another goal of the computations. As the present plate model relies on unmodified three-dimensional strain-stress relations, a particularly interesting case is when, applying low-order approximations, the Poisson's ratio tends to 0.5 and the thickness of the plate tends to zero, simultaneously. The performance of the plate model and the dual-mixed *hp* finite elements on distorted meshes and on plates having curvilinear boundaries is also investigated and presented.

5.1. **Simply supported square plate.** The simply supported square plate of side length $L = 1$ m and thickness $d$ is subjected to a uniformly distributed load $q = 1$ Pa on its middle surface $\bar{S}$. The load is taken into account by prescribing $\widetilde{p}_3^+ = \widetilde{p}_3^- = q/2$ on its top and bottom faces. The material of the plate is isotropic and characterized by its elasticity modulus $E = 30$ GPa and Poisson's ratio $\nu = 0.3$. Three-dimensional benchmark solutions for this plate problem with side-length-to-thickness ratios $L/d = 10$ and $L/d = 100$ can be found in [32], obtained by applying displacement-based $p$-version finite elements. The main objectives of the numerical analysis are (i) the computation of the modeling error of the stress-based plate model and (ii) the performance of the dual-mixed $hp$ plate bending element through the convergence of the relative errors in energy norm. The extrapolated 3D strain energy values reported in [32] are used for comparisons.

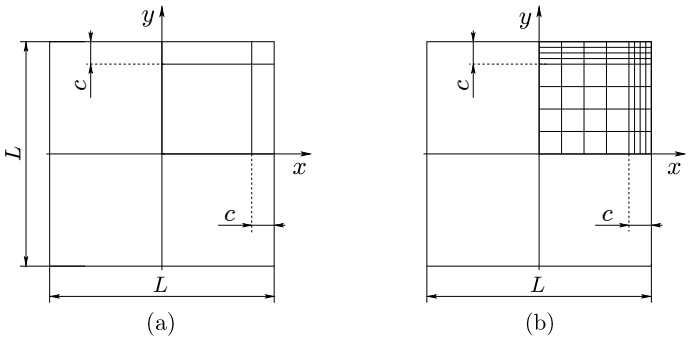


Figure 1. Graded mesh on a square plate with grading parameter $c$

The double symmetry of the problem allows the discretization of one quarter of the plate only. Two meshes are used for the computations: the graded mesh in Figure 1(a) containing $2 \times 2 = 4$ rectangular elements with a grading parameter denoted by $c$, and a refined, $8 \times 8 = 64$ element mesh shown in Figure 1(b), which is obtained by uniform division of each element in Figure 1(a) into 16 elements. Two types of simple supports are considered: soft and hard, according to the definitions given in [32].

5.1.1. *Modeling error computation for soft simple support.* The computations for the modeling error were performed using the 64-element mesh shown in Figure 1(b), applying $p$-extension with polynomial degree $p$ varying from 2 to 9 (see Section 4), where $p$ is the highest polynomial degree used for the approximation of the first-order stress functions in (3.36)–(3.37). The grading parameter is chosen to be $c = 0.1$ for $L/d = 10$, and $c = 0.03$ for $L/d = 100$ (these choices are justified by the investigations presented in Subsection 5.1.2). The convergence of the strain energy and the relative error in the energy norm with respect to the 3D reference solution are summarized in Tables 1 and 2. It can be seen that for $p > 5$, the first eight significant digits of the energy values are the same[1], indicating that the maximum capability of the 2D plate model is reached for this problem. In other words this means that the discretization

[1]The strain energy values in [32] are given in seven significant digits.

Table 1. Square plate, uniform load, soft simple support, $L/d = 10$: relative error in strain energy and in energy norm with respect to the 3D reference solution, $p$-extension on a graded $8 \times 8$ element mesh

| $p$ | strain energy | rel. error in energy (%) | rel. error in energy norm (%) |
|---|---|---|---|
| 2 | 7.0799145 e–7 | 0.625 | 7.90 |
| 3 | 7.0593276 e–7 | 0.332 | 5.76 |
| 4 | 7.0591129 e–7 | 0.329 | 5.73 |
| 5 | 7.0591100 e–7 | 0.329 | 5.73 |
| 6 | 7.0591099 e–7 | 0.329 | 5.73 |
| 7 | 7.0591099 e–7 | 0.329 | 5.73 |
| 8 | 7.0591099 e–7 | 0.329 | 5.73 |
| 9 | 7.0591099 e–7 | 0.329 | 5.73 |
| 3D [32] | 7.035974 e–7 | – | – |

Table 2. Square plate, uniform load, soft simple support, $L/d = 100$: relative error in strain energy and in energy norm with respect to the 3D reference solution, $p$-extension on a graded $8 \times 8$ element mesh

| $p$ | strain energy | rel. error in energy (%) | rel. error in energy norm (%) |
|---|---|---|---|
| 2 | 6.2739339 e–4 | 2.23 e–1 | 4.79 e+0 |
| 3 | 6.2608011 e–4 | 1.98 e–2 | 1.41 e+0 |
| 4 | 6.2599754 e–4 | 6.61 e–3 | 8.13 e–1 |
| 5 | 6.2599455 e–4 | 6.13 e–3 | 7.83 e–1 |
| 6 | 6.2599448 e–4 | 6.12 e–3 | 7.82 e–1 |
| 7 | 6.2599448 e–4 | 6.12 e–3 | 7.82 e–1 |
| 8 | 6.2599448 e–4 | 6.12 e–3 | 7.82 e–1 |
| 9 | 6.2599448 e–4 | 6.12 e–3 | 7.82 e–1 |
| 3D [32] | 6.259562 e–4 | – | – |

error becomes negligible for higher $p$ values (using three significant digits) and the modeling error of the plate model in energy norm is 5.73 % for $L/d = 10$ (reached for $p > 3$) and 0.782 % for $L/d = 100$ (reached for $p > 4$). The comparison of these modeling errors to those of the classical Kirchhoff and Reissner–Mindlin plate models, computed in [32], is given in Table 3.

Table 3. Square plate, uniform load, soft simple support: modeling error in energy norm for different plate models

| $L/d$ | Kirchhoff plate model | Reissner-Mindlin plate model | present plate model |
|---|---|---|---|
| 10 | 34.5% | 11.2% | 5.73% |
| 100 | 9.88% | 2.94% | 0.782% |

5.1.2. *Square plate with soft simple support: p-extension on 4-element meshes.* The capabilities of the stress-based plate model and the related dual-mixed *hp* finite elements are investigated next using the 4-element mesh shown in Figure 1a) with different grading parameters $c$: starting from a uniform mesh with $c = 0.25$, $c$ takes the values of 0.1, 0.05 and 0.03. $p$-extension with polynomial degree $p$ varying from 2 to 9 is applied again.

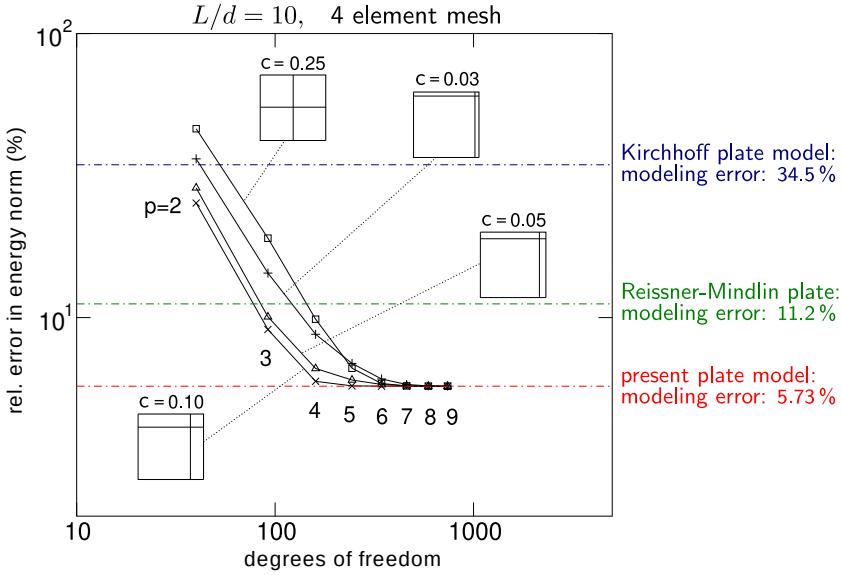


Figure 2. Square plate, uniform load, soft simple support, $L/d = 10$: convergence of the relative error in energy norm with respect to the 3D reference solution; $p$-extension on a $2 \times 2$ element mesh with different grading parameter $c$ and the modeling error of plate models

Figures 2 and 3 show the convergence curves of the relative errors in energy norm with respect to the 3D reference solution for $L/d = 10$ and $L/d = 100$, respectively. Among the four graded meshes applied, the best rate of convergence is achieved when $c = 0.1$ for $L/d = 10$, and $c = 0.03$ for $L/d = 100$. The modeling errors of the different plate models (from Table 3) are illustrated by horizontal lines in the figures.

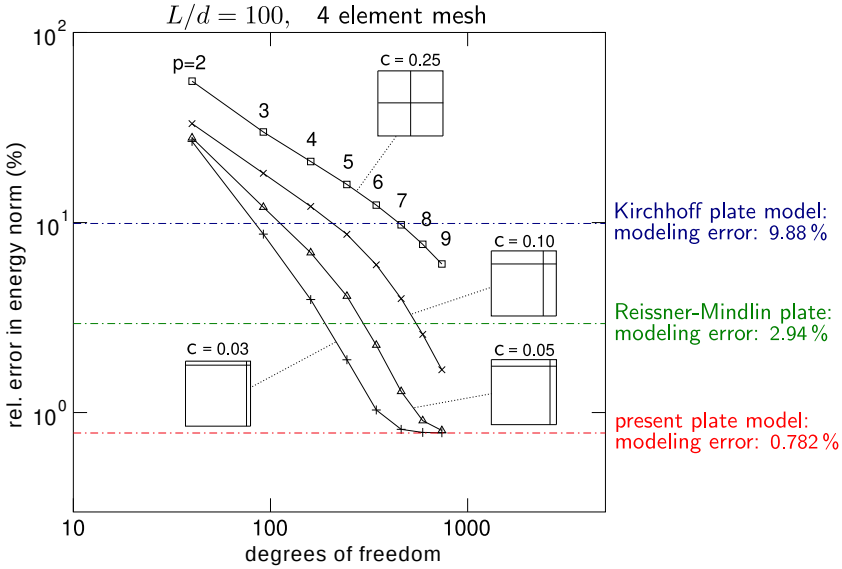


Figure 3. Square plate, uniform load, soft simple support, $L/d = 100$: convergence of the relative error in energy norm with respect to the 3D reference solution; $p$-extension on a $2 \times 2$ element mesh with different grading parameter $c$ and the modeling error of plate models

Figures 2 and 3 indicate that the discretization error can be controlled by $p$-extension even on a 4-element mesh, and the modeling error, computed and tabulated in Table 3 using a 64-element mesh, can be reached on a properly graded 4-element mesh, as well. For $L/d = 10$, the modeling error is reached at higher polynomial degree $p$ for all values of the grading parameter $c$, whereas for $L/d = 100$, the modeling error is reached when $c = 0.03$ and $p > 7$.

5.1.3. *Square plate with hard simple support.* The square plate investigated previously is considered now with hard simple support. The shear locking-free property of the dual-mixed plate bending element developed will be demonstrated through the convergence of the scaled displacement and bending moment defined by

$$\bar{u}_3 = u_3 \frac{10^2 D}{qL^4}, \qquad \bar{M}_{11} = M_{11} \frac{10}{qL^2}, \qquad D = Ed^3/12(1-\nu^2) \tag{5.1}$$

and computed at the center of the plate, where $q$ is the applied load density on the middle surface $\bar{S}$ and $D$ is the flexural rigidity of the plate. The computed values are compared to the Navier-series solution given in [33].

First, the approximation capability of a higher-order element with polynomial degree $p = 8$ is investigated and compared to the exact limit solution for thin plates, given in [33], using a $2 \times 2$ element mesh. In Figure 4, the scaled displacements and bending moments (5.1) are plotted and tabulated for different thicknesses as $d \to 0$. It is seen that as the side-length-to-thickness ratio goes to infinity, the displacements

and bending moments converge to the exact limit solution, indicating that the plate model is asymptotically correct.

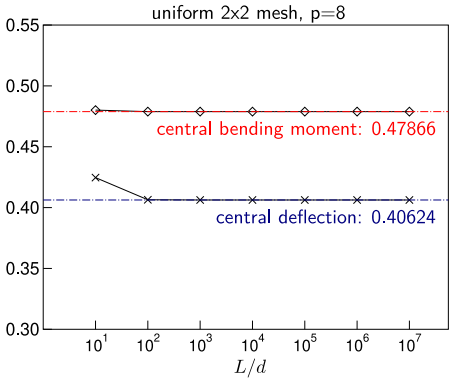


| $L/d$ | $\bar{u}_3$ | $\bar{M}_{11}$ |
|---|---|---|
| 10 | 0.42465 | 0.48011 |
| 100 | 0.40642 | 0.47887 |
| 1 000 | 0.40624 | 0.47886 |
| 10 000 | 0.40624 | 0.47886 |
| 100 000 | 0.40624 | 0.47886 |
| 1 000 000 | 0.40624 | 0.47886 |
| 10 000 000 | 0.40624 | 0.47885 |
| Series [33] | 0.40624 | 0.47886 |

Figure 4. Square plate with hard simple support: scaled displacement $\bar{u}_3$ and bending moment $\bar{M}_{11}$ at the center of the plate as $d \to 0$, uniform $2 \times 2$ element mesh, $p = 8$,

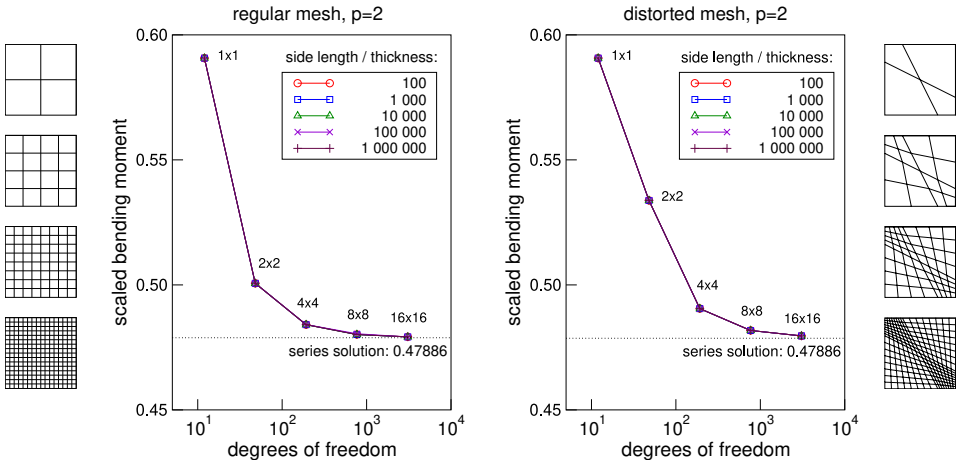


Figure 5. Square plate with hard simple support: convergence of the central bending moment for different side-length-to-thickness ratios applying dual-mixed elements and performing $h$-extension on regular (left) and distorted (right) meshes

Since shear locking is more likely to appear when low-order polynomial approximation is used, especially in the displacement-based models, the capability of the present plate model is investigated next by performing $h$-extension with polynomial degree $p = 2$ kept fixed. Note that $p = 2$ is the lowest possible polynomial degree

in the stress-based plate element developed. Results were obtained by uniform mesh refinement, starting with a single element and ending with a $16 \times 16$ element mesh.

Figure 5 shows the convergence curves for the scaled bending moment at the center of the plate for five different aspect ratios, applying a regular mesh (on the left) and skew mesh with distorted elements (on the right). It is seen that the rates of convergence are not sensitive to the thickness of the plate, whether either regular or distorted elements are used. Practically, the same convergence curve was obtained for all five side-length-to-thickness ratios considered, both for regular and irregular meshes, which indicates that the dual-mixed plate bending element is completely free from shear-locking. The skew mesh gives lower rates of convergence then the regular mesh, independently of the thickness. It is also seen that a good approximation of the exact limit solution can be obtained already with a $16 \times 16$ element mesh at $p = 2$, even for the unrealistic side-length-to-thickness ratio of $10^6$, which corresponds to a plate of thickness $d = 1$ $\mu$m and side length $L = 1$ m.

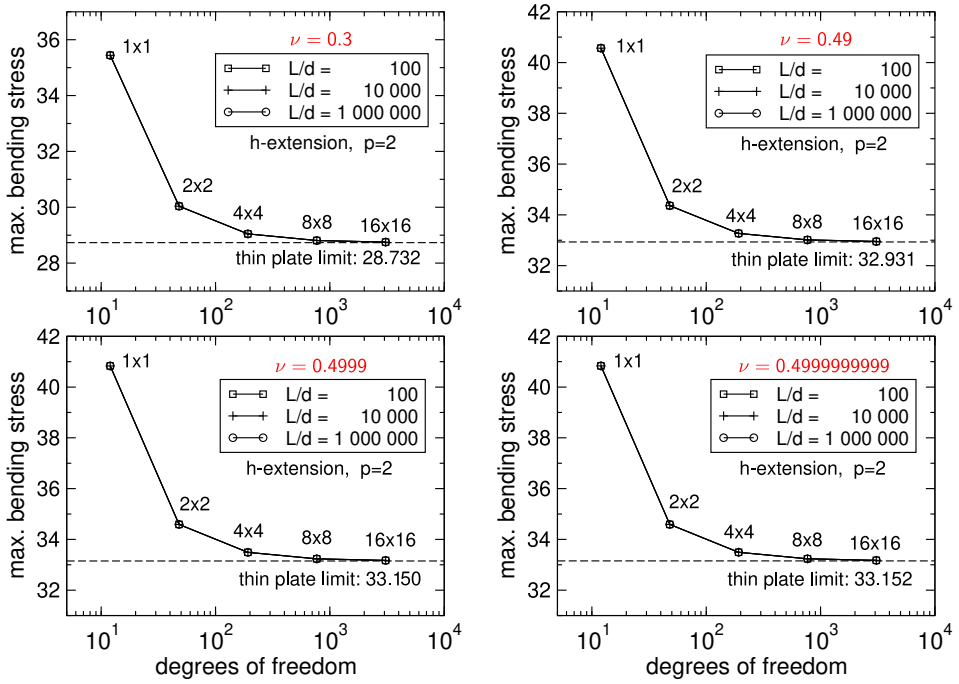


Figure 6. Square plate with hard simple support, dual-mixed element, $h$-extension, uniform mesh refinement: convergence of the central bending stress when the Poisson's ratio approaches 0.5 with simultaneously increased side-length-to-thickness ratio

5.1.4. *Square plate, hard simple support: h-extension with incompressibility constraint.* As the stress-based plate model relies on unmodified three-dimensional strain-stress relations, the computations were also performed by investigating the effect of the

Poisson's ratio, when it approaches to the incompressibility limit of 0.5 and, at the same time, the thickness of the plate goes to zero. Figure 6 shows the results obtained for the convergence of the maximum bending stress as $\nu \to 0.5$ and $d \to 0$, obtained by performing $h$-extension with regular meshes and polynomial degree $p = 2$ kept fixed. The diagrams in Figure 6 clearly indicate that the rates of convergence of the dual-mixed element is perfectly insensitive to the values of the Poisson's ratio and the thickness of the plate, i.e., the element is free from both shear locking and incompressibility locking. It can also be seen from Figure 6 that the thin plate limit values for different Poisson's ratios, computed from the Navier-series solution given in [33], are approximated well by applying a $16 \times 16$ element mesh, independently of the values of the Poisson's ratio $\nu$ and the thickness $d$.

5.2. **Thin circular plate with hard clamp and soft simple support.** In this example the classical problem of a circular plate is investigated in order to test the performance of the stress-based plate model and the dual-mixed $hp$ finite elements on domains containing curved boundaries. The plate, made of isotropic material, is subjected to a uniformly distributed load $q = 1$ Pa on its middle surface $\bar{S}$. The radius of the plate is $R = 0.5$ m, the elasticity modulus is $E = 109.2$ GPa and the Poisson's ratio is $\nu = 0.3$. Two types of boundary condition are investigated: hard clamp and soft simple support.

One quarter of the plate is discretized only with prescribed symmetry conditions on the edges of symmetry. When $h$-extension is performed, a four-step mesh refinement shown in Figure 7 is applied by keeping $p = 2$ constant. For $p$-extensions, the 3-element mesh shown in Figure 7 is used. The exact mapping of the elements with curved edges was performed using the blending function method [9].

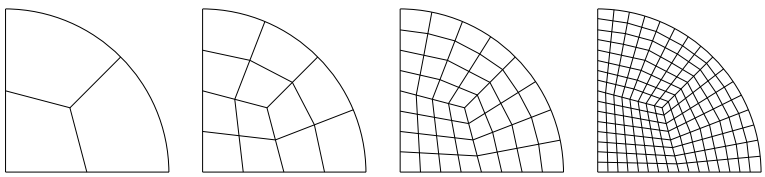

Figure 7. Circular plate problem: the mesh refinement used for $h$-extension

Applying hardly clamped boundary conditions, the analytic solutions for the central displacement and the boundary shear force are [34]

$$u_3 = \frac{qR^4}{64D}, \qquad Q = \frac{qR}{2}, \tag{5.2}$$

where $D$ is given by $(5.1)_3$. For numerical comparisons, the scaled analytic displacement $\bar{u}_3 = u_3 10^2 D/qR^4 = 1.565$ is used. The convergences of the scaled central displacement and the shear force at the boundary are plotted in Figure 8, for both $h$- and $p$-extensions, when the diameter-to-thickness ratio is increased from $10^3$ to $10^6$.

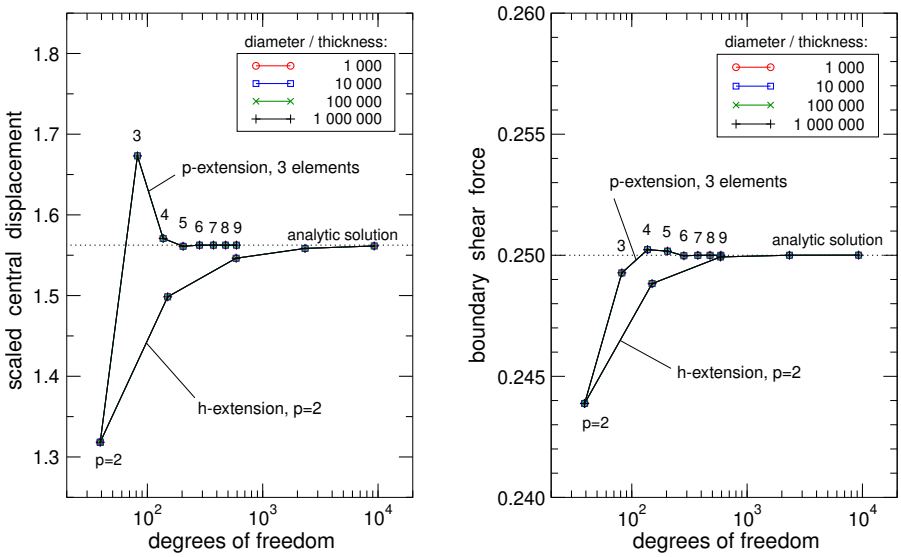


Figure 8. Hardly clamped circular plate: convergence of the scaled central displacement and the shear force at the boundary

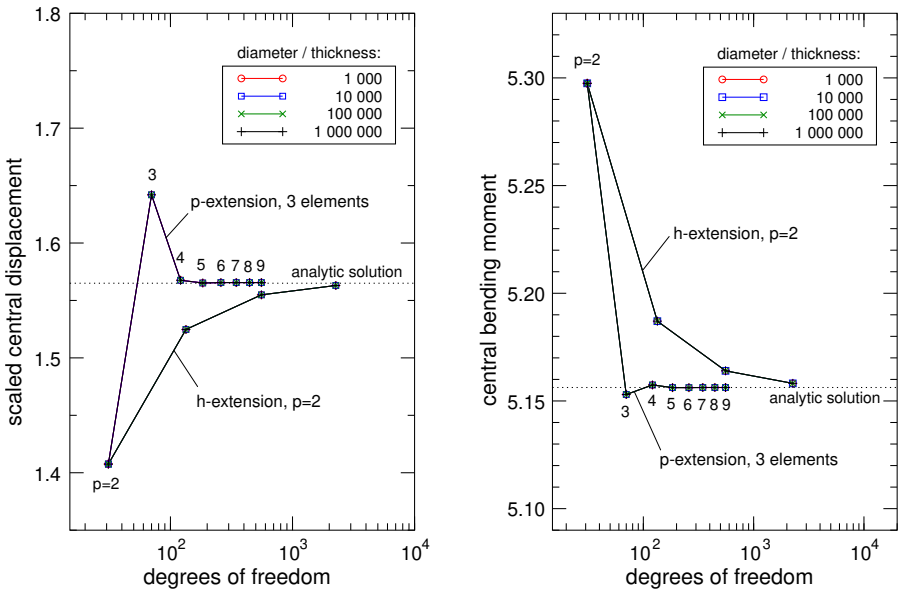


Figure 9. Simply supported circular plate: convergence of the scaled displacement and the bending moment at the center of the plate

When soft simple support is applied, the analytic solutions for the displacement and the bending moment at the center of the plate are [35]

$$u_3 = \frac{qR^4}{64D}\frac{5+\nu}{1+\nu}, \qquad M = \frac{qR^2}{16}(3+\nu), \tag{5.3}$$

where $D$ is defined by $(5.1)_3$. For numerical comparisons, the scaled analytic displacement $\bar{u}_3 = u_3\, 10^2 D(1+\nu)/qR^4(5+\nu) = 1.565$ is used. Figure 9 shows the convergence of the scaled central displacement and the central bending moment for both $h$- and $p$-extensions, considering four diameter-to-thickness parameters with decreasing plate thickness $d$.

It can be seen from Figures 8 and 9 that the thickness change has no influence at all for the rates of convergences, either the displacement or the shear force or the bending moment is considered. This property seems to be independent of the applied boundary conditions as well. As expected, the $p$-extension on the three-element mesh gives much faster convergence for each variable than the mesh refinement with polynomial degree $p = 2$ kept fixed.

5.3. **Clamped square plate with a circular hole.** The last example is a square plate of side length $L = 2$ m with a central hole of radius $r = 0.2$ m (Figure 10). The thickness of the plate is 0.1 m, the side-length-to-thickness ratio is $L/d = 20$. The outer edge of the plate is clamped, the boundary of the circular hole is traction-free. The plate, made of isotropic material, is subjected to a uniformly distributed load with intensity $q = 1$ Pa on its middle surface. The elasticity modulus is $E = 30$ GPa and the Poisson's ratio is $\nu = 0.3$.

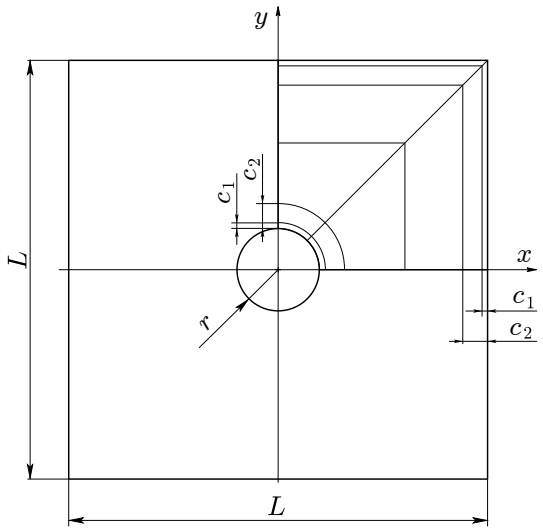


Figure 10. Clamped square plate with a circular hole and the graded 16 element mesh

A solution for this plate problem, considering a hierarchic sequence of displacement-based plated models, and the modeling error computation with respect to the 3D finite element solution can be found in [36]. The 3D solution given in [36] is considered here as a reference solution. All the computations were performed on one-quarter of the plate applying a 12-element graded mesh, shown in Figure 10. The strain energy computations correspond to this sub-domain as well. The same mesh used in [36] is applied here, the grading parameters of $c_1 = 0.03$ m and $c_2 = 0.11$ m (see Figure 10) take into account the boundary layers at the inner and outer edges of the plate. Note that the mesh contains elements with curved boundaries and straight edges as well. The blending function method [9] is used for exact mapping of the elements with curved edges.

Performing $p$-extension with polynomial degree $2 \leq p \leq 9$, the convergence of the strain energy and the relative discretization error in energy norm, with respect to the estimated exact strain energy of the plate model, as well as the rates of convergence in energy norm are shown in Table 4. The extrapolated exact strain energy (corresponding to $p = \infty$) of the plate model was computed from the solutions at $p = 7, 8, 9$, according to the a posteriori error estimation method described in [9].

Table 4. Clamped square plate with a central hole, uniform load, $L/d = 20$: convergence of the strain energy and the discretization error in energy norm with the rates of convergence on a graded 12 element mesh using the dual-mixed plate element with $p$-extension

| $p$ | DOF | strain energy | rel. error in energy norm (%) | rate of convergence |
|---|---|---|---|---|
| 2 | 138 | 6.533638028 e−7 | 4.160 e+1 | – |
| 3 | 300 | 5.603839912 e−7 | 7.841 e+0 | 2.15 |
| 4 | 510 | 5.570927830 e−7 | 1.544 e+0 | 3.06 |
| 5 | 768 | 5.569858174 e−7 | 6.815 e−1 | 2.00 |
| 6 | 1074 | 5.569640950 e−7 | 2.729 e−1 | 2.73 |
| 7 | 1428 | 5.569606279 e−7 | 1.106 e−1 | 3.17 |
| 8 | 1830 | 5.569601009 e−7 | 5.258 e−2 | 3.00 |
| 9 | 2280 | 5.569599881 e−7 | 2.720 e−2 | 3.00 |
| $\infty$ | | 5.569599469 e−7 | – | – |

The convergences of the strain energy and the relative error in the energy norm with respect to the 3D reference solution of [36] are given in Table 5. It can be seen that the discretization error becomes negligible for $p > 7$ (using 4 significant digits of precision), and the relative error of 8.000% is the modeling error of the stress-based plate model for this problem. In Table 6, the modeling error of the present plate model is compared to those of two higher-order displacement-based plate models, referred as $(1, 1, 2)$ and $(3, 3, 2)$ in the hierarchic sequence of models in [36] (the numbers in parentheses refer to the polynomial degree of the three displacement components in

Table 5. Clamped square plate with a central hole, uniform load, $L/d = 20$: relative errors in strain energy and in energy norm with respect to the 3D reference solution on a graded 12 element mesh using the dual-mixed plate element with $p$-extension

| $p$ | strain energy | rel. error in energy (%) | rel. error in energy norm (%) |
|---|---|---|---|
| 2 | 6.533638028 e –7 | 1.799 e+1 | 42.50 |
| 3 | 5.603839912 e –7 | 1.259 e+0 | 11.22 |
| 4 | 5.570927830 e –7 | 6.640 e –1 | 8.149 |
| 5 | 5.569858174 e –7 | 6.446 e –1 | 8.029 |
| 6 | 5.569640950 e –7 | 6.407 e –1 | 8.005 |
| 7 | 5.569606279 e –7 | 6.401 e –1 | 8.001 |
| 8 | 5.569601009 e –7 | 6.400 e –1 | 8.000 |
| 9 | 5.569599881 e –7 | 6.400 e –1 | 8.000 |
| $\infty$ | 5.569599469 e -7 | 6.400 e –1 | 8.000 |
| 3D [36] | 5.534181949 e –7 | – | – |

the thickness direction). The results indicate that the seven-field stress-based plate model gives better modeling error than the seven-field displacement-based $(1, 1, 2)$ model, but is not as accurate as the eleven-field $(3, 3, 2)$ model.

Table 6. Clamped square plate with a central hole, uniform load, $L/d = 20$: comparison of the modeling errors in energy norm for two higher-order displacement-based plate models and the stress-based plate model

| plate model | strain energy | modeling error in energy norm (%) |
|---|---|---|
| (1, 1, 2) [36] | 5.463957687 e –7 | 11.26 |
| (3, 3, 2) [36] | 5.512825921 e –7 | 6.212 |
| present | 5.569599881 e –7 | 8.000 |
| 3D [36] | 5.534181949 e –7 | – |

The convergences of the bending moments $M_x(L/2, 0)$ and $M_y(L/2, 0)$ at the mid-point of the outer boundary are shown in Figure 11, performing $p$-extension. It is seen that the convergence of the bending moments is very fast and their computed values for $p > 4$ are very close to the limiting values, computed as the average values of the solutions with polynomial degrees $p = 7, 8, 9$.

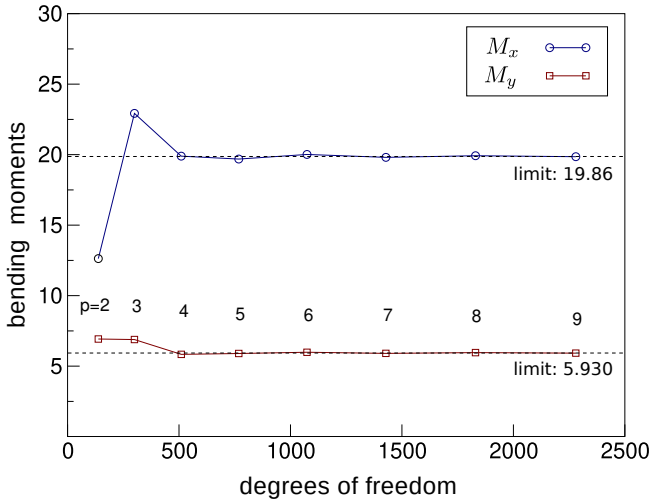


Figure 11. Clamped square plate with a central hole, uniform load, $L/d = 20$: convergence of the bending moments at the midpoint of the outer edge of the plate, performing $p$-extension

## 6. Concluding remarks

A stress-based dimensional reduction procedure has been presented for elastic plates and a related dual-mixed *hp*-version plate bending finite element model has been developed. The derivation of the plate model and the construction of the elements were based on the linearized weak forms of the kinematic equation and the angular momentum balance equation of three-dimensional non-linear elasticity. The independent variables in the formulation are the three-dimensional stresses and rotations. Their expansion into truncated power series with respect to the thickness coordinate and the satisfaction of the expanded translational equilibrium equations by the introduction of first-order stress functions have led to a seven-field dimensionally reduced plate model. Out of the seven fields, three fields describe the membrane problem and four fields describe the plate bending problem. Stable approximation spaces for the stress function and rotation components have been chosen by utilizing the analogy between the weak forms of the membrane and the bending models of the present formulation and the displacement-pressure formulation of elasticity. The plate model and the *hp* finite elements employ unmodified three-dimensional strain-stress relations.

The main interest in the numerical analysis and comparisons was twofold: firstly, the computation of the modeling error of the stress-based plate model and, secondly, the justification of the locking-free behavior of the dual-mixed finite elements. The first goal could be achieved by applying the $p$-extension capabilities of the element model. In the case of the problem of a uniformly loaded square plate it was shown that the modeling error of the present plate model is better than the classical displacement based first-order plate theories. The modeling error of the stress-based plate model

was also compared to those of higher-order displacement-based models by solving the problem of a square plate with a central circular hole. The locking-free property of the formulation and the dual-mixed plate bending elements has been justified numerically for both $h$- and $p$-extensions by investigating the model problems of a square plate under uniform load with soft and hard simple support and a uniformly loaded circular plate with hard clamp and soft simple support. It was confirmed that the convergence properties of the $hp$ dual-mixed elements are insensitive to the thickness change and to the value of the Poisson's ratio, i.e., the finite element model has been proved to be free from shear locking and incompressibility locking when either low-order $h$-, or higher-order $p$-version elements were applied.

## References


1. Reddy, J. N. *Theory and Analysis of Elastic Plates and Shells*. 2nd. Boca Raton: CRC Press, 2007. DOI: 10.1201/9780849384165.
2. Bishoff, M., Wall, W. A., Bletzinger, K. U., and Ramm, E. *Models and Finite Elements for Thin-Walled Structures. In: The Encyclopedia of Computational Mechanics Vol. II* (E. Stein, R. de Borst and T. J. R. Hughes, Eds.) pp. 59–137. New York: John Wiley & Sons, 2004. DOI: 10.1002/0470091355.ecm026.
3. Chapelle, D. and Bathe, K. J. *The Finite Element Analysis of Shells – Fundamentals*. 2nd. Berlin: Springer-Verlag, 2011.
4. Yang, H. T. Y., Saigal, S., Masud, A., and Kapania, R. K. "A survey of recent shell finite elements." *International Journal for Numerical Methods in Engineering,* **47**, (2000), pp. 101–127. DOI: 10.1002/(SICI)1097-0207(20000110/30)47:1/3<101::AID-NME763>3.0.CO;2-C.
5. Cen, S. and Shang, Y. "Developments of Mindlin-Reissner plate elements." *Mathematical Problems in Engineering,* Article ID 456740 (2015), pp. 3–61. DOI: 10.1155/2015/456740.
6. Hakula, H., Leino, Y., and Pitkäranta, J. "Scale resolution, locking, and high-order finite element modelling of shells." *Computer Methods in Applied Mechanics and Engineering,* **133**, (1996), pp. 157–182. DOI: 10.1016/0045-7825(95)00939-6.
7. Szabó, B. A. and Sahrmann, G. J. "Hierarchic plate and shell models based on $p$-extension." *International Journal for Numerical Methods in Engineering,* **26**, (1988), pp. 1855–1881. DOI: 10.1002/nme.1620260812.
8. Arciniega, R. A. and Reddy, J. N. "Tensor-based finite element formulations for geometrically nonlinear analysis of shells." *Computer Methods in Applied Mechanics and Engineering,* **196**, (2007), pp. 1048–1073. DOI: 10.1016/j.cma.2006.08.014.
9. Szabó, B. and Babuška, I. *Introduction to Finite Element Analysis. Formulation, Verification and Validation*. New York: John Wiley & Sons, 2011.
10. Bathe, K. J. *Finite Element Procedures*. Upper Saddle River, New Jersey: Prentice-Hall, 1996. DOI: 10.1002/nme.1620190115.

11. Hauptmann, R. and Schweizerhof, K. "A systematic development of 'solid-shell' element formulations for linear and non-linear analyses employing only displacement degrees of freedom." *International Journal for Numerical Methods in Engineering,* **42**, (), pp. 49–69. doi: 10.1002/(SICI)1097-0207(19980515)42:1<49::AID-NME349>3.0.CO;2-2.
12. Wei, G., Lardeur, P., and Druesne, F. "Solid-shell approach based on first-order or higher-order plate and shell theories for the finite element analysis of thin to very thick structures." *European Journal of Mechanics - A/Solids,* **94**, 104591, (2022). doi: 10.1016/j.euromechsol.2022.104591.
13. Boffi, D., Brezzi, F., and Fortin, M. *Mixed and Hybrid Finite Element Methods and Applications*. New York: Springer-Verlag, 2013. doi: 10.1007/978-3-642-36519-5.
14. Wiśniewski, K. *Finite Rotation Shells: Basic Equations and Finite Elements for Reissner Kinematics. Lecture Notes on Numerical Methods in Engineering and Sciences*. Dordrecht: CIMNE-Springer, 2010. doi: 10.1007/978-90-481-8761-4.
15. Fraeijs de Veubeke, B. M. "Stress function approach." *Proceedings of the World Congress on Finite Element Methods*. Bournemouth, U.K., 1975, J.1–J.51.
16. Fraeijs de Veubeke, B. M. and Millard, A. "Discretization of stress fields in the finite element method." *Journal of the Franklin Institute,* **302**, (1976), pp. 389–412. doi: 10.1016/0016-0032(76)90032-6.
17. Fraeijs de Veubeke, B. M. "Discretization of rotational equilibrium in the finite element method." *Lecture Notes in Mathematics. Proceedings of the Mathematical Aspects of Finite Element Methods held in Rome, December 10–12, 1975*. Ed. by I. Galligiani and E. Magenes. Vol. 606. Berlin: Springer-Verlag, 1977, pp. 87–112.
18. Roberts, J. E. and Thomas, J. M. Mixed and Hybrid Methods. In: *Handbook of Numerical Analysis, Vol. II* (P. G. Ciarlet and J. L. Lions, Eds.) Amsterdam: North-Holland, 1991, pp. 523–639.
19. Bertóti, E. "Dual-mixed *p* and *hp* finite element methods for elastic membrane problems." *International Journal for Numerical Methods in Engineering,* **53**, (2002), pp. 3–29. doi: 10.1002/nme.389.
20. Kocsán, L. G. "Derivation of a dual-mixed *hp*-finite element model for axisymmetrically loaded cylindrical shells." *Archive of Applied Mechanics,* **81**, (2011), pp. 1953–1971. doi: 10.1007/s00419-011-0530-3.
21. Tóth, B. "Dual-mixed *hp* finite element model for elastic cylindrical shells." *ZAMM Journal of Applied Mathematics and Mechanics,* **92**, (2012), pp. 236–252. doi: 10.1002/zamm.201100044.
22. Tóth, B. and Kocsán, L. G. "Comparison of dual-mixed *h*- and *p*-version finite element models for axisymmetric problems of cylindrical shells." *Finite Element in Analysis and Design,* **65**, (2013), pp. 50–62. doi: 10.1016/j.finel.2012.11.002.

23. Tóth, B. "Hybridized dual-mixed *hp*-finite element model for shells of revolution." *Computers and Structures,* **218**, (2019), pp. 123–151. DOI: 10.1016/j.compstruc.2019.03.003.
24. Tóth, B. "Natural frequency analysis of shells of revolution based on hybrid dual-mixed *hp*-finite element formulation." *Applied Mathematical Modelling,* **98**, (2021), pp. 722–746. DOI: 10.1016/j.apm.2021.06.001.
25. Ogden, R. W. *Non-Linear Elastic Deformations.* (2nd ed., Dover, Mineola, 1997). Chichester: Ellis Horwood, 1984.
26. Atluri, S. N. and Cazzani, A. "Rotations in computational solid mechanics." *Archives of Computational Methods in Engineering,* **2**, (1995), pp. 49–138. DOI: 10.1007/BF02736189.
27. Géradin, M. and Cardona, A. *Flexible Multibody Dynamics. A Finite Element Approach.* Chichester, England: John Wiley & Sons, 2001.
28. Fraeijs de Veubeke, B. M. "A new variational principle for finite elastic displacements." *International Journal for Engineering Sciences,* **10**, (1972), pp. 745–763. DOI: 10.1016/0020-7225(72)90079-1.
29. Bertóti, E. "Indeterminacy of first-order stress functions and the stress- and rotation-based formulation of linear elasticity." *Computational Mechanics,* **14**, (1994), pp. 249–265. DOI: 10.1007/BF00370076.
30. Wiśniewski, K. and Turska, E. "Kinematics of finite rotation shells with in-plane twist parameter." *Computer Methods in Applied Mechanics and Engineering,* **190**(8), (2000), pp. 1117–1135. DOI: 10.1016/S0045-7825(99)00469-7.
31. Stenberg, R. and Suri, M. "Mixed *hp* finite element methods for problems in elasticity and Stokes flow." *Numerische Mathematik,* **72**, (1996), pp. 367–389. DOI: 10.1007/s002110050174.
32. Babuška, I. and Scapolla, T. "Benchmark computation and performance evaluation for a rhombic plate bending problem." *International Journal for Numerical Methods in Engineering,* **28**, (1989), pp. 155–179. DOI: 10.1002/nme.1620280112.
33. Timoshenko, S. P. and Woinowsky-Krieger, S. *Theory of Plates and Shells.* 2nd. New-York: McGraw-Hill, 2007.
34. Szilard, R. *Theory and analysis of plates.* NJ: Prentice-Hall: Englewood Cliffs, 1974.
35. Budynas, R. G. and Sadegh, A. M. *Roark's Formulas for Stress and Strain.* (9th edition). New York: McGraw-Hill, 2020.
36. Schwab, C. "A-posteriori error estimation for hierarchic plate models." *Proceedings of the EUROMECH 302 Conference.* Ed. by E. Sanchez-Palencia. Paris, 1993, pp. 1–21.